

A 3D Non-Stationary MIMO Channel Model for Reconfigurable Intelligent Surface Auxiliary UAV-to-Ground mmWave Communications

Baiping Xiong, Zaichen Zhang, *Senior Member, IEEE*,

Hao Jiang, *Member, IEEE*, Jiangfan Zhang, *Member, IEEE*,

Liang Wu, *Member, IEEE* and Jian Dang, *Senior Member, IEEE*,

Abstract

Unmanned aerial vehicle (UAV) communications exploiting millimeter wave (mmWave) can satisfy the increasing data rate demands for future wireless networks owing to the line-of-sight (LoS) dominated transmission and flexibility. However, the LoS link can be easily and severely blocked due to poor propagation environments such as tall buildings and trees. To this end, we introduce a reconfigurable intelligent surface (RIS), which passively reflects signals with programmable reflection coefficients, between the transceivers to enhance the communication quality. Specifically, in this paper we generalize a three-dimensional (3D) non-stationary wideband end-to-end channel model for RIS auxiliary UAV-to-ground mmWave multiple-input multiple-output (MIMO) communication systems. By modeling the RIS as a virtual cluster, we study the *power delivering capability* of RIS as well as the *fading characteristic*

This work is supported by NSFC projects (61960206005, 61971136, 61803211, and 61871111), Jiangsu NSF project (BK20191261), Zhejiang Lab (No. 2019LC0AB02), the Fundamental Research Funds for the Central Universities, and Research Fund of National Mobile Communications Research Laboratory, Southeast University. (*Corresponding author: Zaichen Zhang.*)

B. Xiong, Z. Zhang, L. Wu, and J. Dang are with the National Mobile Communications Research Laboratory, Southeast University, Nanjing 210096, P. R. China. Z. Zhang is also with the Purple Mountain Laboratory, Nanjing 211111, P. R. China. (e-mails: xiongbp@seu.edu.cn; zczhang@seu.edu.cn; wuliang@seu.edu.cn; dangjian@seu.edu.cn).

H. Jiang is with the College of Artificial Intelligence, Nanjing University of Information Science and Technology, 210044, P. R. China; and also with the National Mobile Communications Research Laboratory, Southeast University, Nanjing 210096, P. R. China. (e-mail: jianghao@nuist.edu.cn).

J. Zhang is with the Department of Electrical and Computer Engineering, Missouri University of Science and Technology, Rolla, MO 65409, USA (e-mail: jiangfanzhang@mst.edu).

of the proposed channel model. Important channel statistical properties are derived and thoroughly investigated, and the impact of different RIS reflection phase controlling mechanisms on these statistical properties is studied, which yields some helpful results. The agreement between theoretical and simulated as well as measurement results validate the effectiveness of the proposed channel model.

Index Terms

Reconfigurable intelligent surface, non-stationary mmWave channel model, UAV, reflection phase, statistical properties.

I. INTRODUCTION

Recently, the research on next generation wireless networks has attracted many attentions from both academia and industry, among which the space-air-ground integrated network (SAGIN) has been considered promising to realize global coverage [1], [2]. As an integral part of the SAGIN, unmanned aerial vehicle (UAV) communications have been in rapid development for both civil and military applications due to its low cost and flexibility [3]. Meanwhile, the advantages of applying millimeter wave (mmWave) in terrestrial communications have also motivated the usage of mmWave in UAV communications to satisfy the increasing bandwidth and data rate demands [4]. UAV communications exploiting mmWave will significantly boost the system throughput because of the line-of-sight (LoS) dominated transmission, which, however, can be easily and severely deteriorated when the LoS link gets blocked. Thanks to the development of meta-surface, reconfigurable intelligent surface (RIS), which has the ability to manipulate the impinging waves towards the destinations constructively, has been considered promising to address this issue in a low-cost and energy efficient manner [5], whose design and performance evaluation require an accurate and in-depth understanding of the channel propagation characteristics.

A. Prior Work

Owing to the potential of RIS, there have been many efforts on the integration of RIS in UAV and mmWave communications, respectively. Specifically, by jointly designing the UAV's trajectory and passive beamforming of RIS, the authors in [6] maximized the average achievable rate of a RIS-assisted UAV communication system for obtaining substantially communication quality improvement. The authors in [7] achieved panoramic signal reflection of RIS by deploying the

RIS in the aerial platform; however, they assumed a uniform linear array (ULA) configured RIS, which is hard to implement for the RIS with a large number of units. Moreover, in [8], the authors studied the hybrid precoding design of a RIS aided multi-user mmWave communication system, where the results show desirable performance gain in symbol error rate with the assistance of RIS. The channel capacity of a RIS-assisted indoor mmWave communication system is optimized in [9]. However, the model in [9] was designed for two-dimensional (2D) propagation scenarios and only considered the propagation through RIS. Apart from the aforementioned optimizations of the RIS reflecting phases for UAV and mmWave systems, transceiver design based on RIS architectures for cost effective communications was discussed in [10]. RIS aided non-orthogonal multiple access (NOMA) network for energy efficient communications was studied in [11]. RIS-based index modulation for achieving spectral efficient communications in the context of beyond multiple-input multiple-output (MIMO) solutions was proposed in [12]. Moreover, the potential of terminal position as well as joint localization and communication using RISs were thoroughly investigated in [13] and [14], respectively.

It is worth mentioning that the development of any wireless communication technologies requires an in-depth understanding of the underlying channel characteristics. Thus far, there have been several research results on the path loss modeling of RIS systems [15]- [18], whereas the studies on multipath small-scale statistical RIS channel modeling are still in infancy, let alone the channel modeling for RIS auxiliary UAV mmWave communications. By partitioning the large RIS into tiles, [19] developed a statistical channel model, which, however, ignored the practical orientation angle of RIS. The authors in [20] presented a three-dimensional (3D) non-stationary channel model for RIS-assisted MIMO systems. Nevertheless, the model in [20] was for sub-6 GHz terrestrial communications scenarios. In [21], the authors developed a statistical channel model for RIS-assisted mmWave communications; however, the model was restricted for narrowband stationary systems. These channel models, however, cannot be adapted for RIS auxiliary UAV mmWave communications due to the unique propagation characteristics. In general, the UAV flies in 3D space, thus causes the non-stationarity of the channel. The mmWave channels are typical sparsely-scattered with small angle spread, which leads to the sparsity of the channel. Moreover, the RIS simply reflect the signals by attaching with programmable coefficients without processing, which is significantly different from the relay systems. These all should be carefully considered in RIS auxiliary UAV mmWave channel modeling.

B. Motivations

The channel models in aforementioned studies, which are mainly based on simplistic mathematical models with the channel coefficients generated by complex Gaussian random variables, will suffer from a lack of accuracy and generality to describe the realistic RIS auxiliary UAV communication environments. It is worth mentioning that the RIS, which has no sensing capability, generally reflect the waves without further processing, and only the end-to-end propagation statistics between the transceiver are of interest in algorithm validation and system design. Furthermore, UAV communications at mmWave bands have shown fascinating advantages; however, the corresponding channel properties when incorporating with RIS still remains unknown. These motivate us to study the sparks when RIS meets with UAV mmWave communications and develop efficient statistical channel models to characterize the end-to-end statistics of realistic RIS auxiliary UAV mmWave communication channels.

C. Main Contributions

In this paper, we develop a 3D non-stationary wideband MIMO channel model for RIS auxiliary UAV-to-ground mmWave communications. The major contributions and novelties of this paper are summarized as follows:

- We develop a 3D non-stationary wideband MIMO UAV channel model at mmWave bands for multipath small-scale fading of the propagation channel between the UAV and ground MR with the assistance of RIS, which has the ability to capture the non-stationary properties of UAV channels and sparsity of mmWave channels. By appropriately adjusting the model parameters, the proposed channel model can be adapted for various RIS-assisted communication scenarios.
- Different from existing RIS-assisted channel models, the proposed channel model considers an end-to-end propagation model from the UAV to MR by modeling the RIS as virtual cluster and RIS units as virtual scatterers. In this case, different RIS units share similar distances and angles. It should be noted that although we are modeling the RIS as virtual cluster, the RIS is distinguished from the conventional clusters in [22] and [23] owing to the programmability of RIS reflection coefficients. Then, we show that the proposed channel model is characterized by Rician fading under optimal and discrete reflection phase configurations, whereas by Rayleigh fading under random uniform reflection phase configuration.

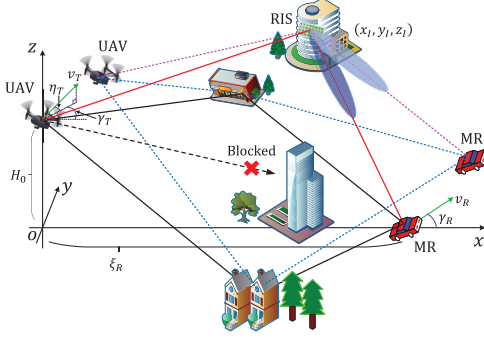


Fig. 1. A physical illustration of the proposed 3D MIMO communication channel model for RIS auxiliary UAV mmWave communications. The direct path between UAV and MR is blocked.

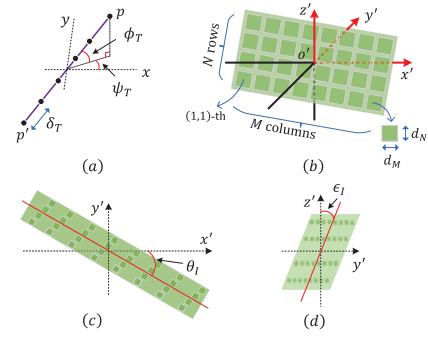


Fig. 2. Definitions of the 3D orientation angles. (a) orientation angles of UAV/MR ULAs; (b) 3D view of RIS; (c) horizontal rotation angle of RIS; (d) vertical rotation angle of RIS.

- The power delivering capability of RIS is investigated, which embodies helpful guidelines for the practical design and deployment of RIS. Perfect agreement between theoretical and simulated as well as measurement results validate the proposed model. The results highlight the advantage of discrete configuration of the RIS reflection phases.

The remainder of this paper is organized as follows. Section II presents the system channel model, where a 3D non-stationary UAV-to-ground mmWave channel model with the assistance of RIS is proposed. In Section III, the important statistical properties of the proposed channel model are derived and analyzed. The results and discussions are presented in Section IV. Finally, we drawn conclusions in Section V.

Notation: Throughout this paper, non-boldface, boldface lowercase, and boldface uppercase letters denote scalar, vector, and matrix, respectively; $|\cdot|$, $\|\cdot\|$, $(\cdot)^T$, and $(\cdot)^*$ stand for absolute value, ℓ_2 norm, transpose, and complex conjugate, respectively; $\mathbb{E}(\cdot)$, $Var(\cdot)$, $\text{Re}(\cdot)$, $\text{Im}(\cdot)$, and $\text{Cov}(\cdot)$ take the expectation, variance, real part, imaginary part, and covariance, respectively.

II. SYSTEM CHANNEL MODEL

As shown in Fig. 1, let us consider a UAV MIMO communication scenario at mmWave frequency bands, where the direct propagation path between the UAV and ground MR is severely blocked due to the poor propagation environments, like buildings and trees. Therefore, we introduce a RIS between the UAV and MR, which aims at enhancing the communication quality. The geometry-based stochastic models (GBSMs) are helpful to provide a mathematical

description of the underlying propagation environments by exploiting available geometrical information and have been widely used in standardized channel models [24]. The proposed wideband channel model also follows the GBSM-based approach to describe the multipath propagations between the UAV and MR, where the UAV and MR are both equipped with 3D positioned omni-directional ULAs with antenna spacings δ_T and δ_R , respectively. The UAV is moving in the air with speed v_T , elevation direction η_T , and azimuth direction γ_T , whereas the MR is moving on the ground with speed v_R and direction γ_R . At the initial instant, that is, $t = 0$, we define the projection of the center of UAV's ULA as the origin of the coordinate system, the line connecting the origin and the center of MR's ULA as the x -axis, the z -axis is vertical upward, and thus the y -axis can be obtained based on the right-hand rule. Then, the initial locations of the central points of UAV's ULA, RIS, and MR's ULA can be expressed as $(0, 0, H_0)$, (x_I, y_I, z_I) , and $(\xi_R, 0, 0)$, respectively. In the following, we adopt the planar wavefront assumption due to the fact that the dimensions of the ULAs and RIS are much smaller than the propagation distances [25]. This leads to different antenna elements in the same ULA and different RIS units sharing the same signal direction. As shown in Fig. 2(a), the azimuth and elevation orientation angles of the 3D positioned UAV's ULA are denoted by ψ_T and ϕ_T , respectively, whereas at the MR, they are denoted by ψ_R and ϕ_R , respectively. Moreover, we consider the RIS with MN reflecting units, which is composed of M columns (counting from left to right) and N rows (counting from bottom to top), as shown in Fig. 2(b). The size of each unit, that is, $d_M \times d_N$, is usually of sub-wavelength scale, typically ranging from $1/10$ to $1/2$ of the wavelength, while the gaps between two adjacent units are generally much smaller than the dimension of the unit, and hence are ignored in the following discussions [18]. It is worth mentioning that the existing literature generally assumed the RIS surface being perpendicular to the ground and do not consider the orientations of RIS, which, in principle, will limit the scope of the models. To address this limitation, we introduce a horizontal rotation angle θ_I and a vertical rotation angle ϵ_I to describe the practical orientations of RIS, which enhances the generality of the proposed channel model and boosts the accuracy of the proposed channel model to describe the realistic RIS auxiliary communication environments, as shown in Fig. 2(b)-(d). Note that the three axes in the local coordinate system $x'-y'-z'$ in Fig. 2(b) are parallel to those in the global coordinate system $x-y-z$ in Fig. 1. The orientations of the UAV's and MR's ULAs are fixed, whereas the orientation of RIS can be optimized to meet the requirements in different communication conditions, which,

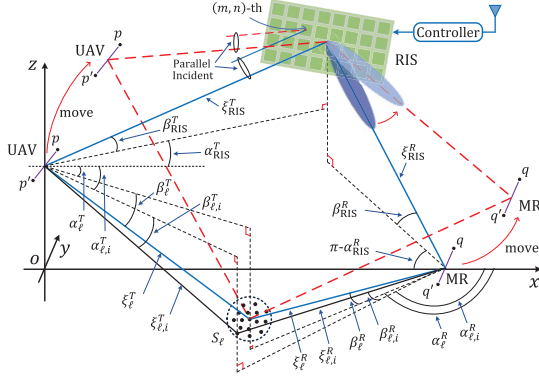


Fig. 3. A visualized illustration of the proposed RIS-assisted UAV channel model. For clarify, only cluster S_ℓ is shown.

| | |
|---|---|
| $\xi_{\text{RIS}}^T(t), \xi_{\text{RIS}}^R(t)$ | distances between UAV/MR and RIS |
| $\xi_\ell^T(t), \xi_\ell^R(t)$ | distances between UAV/MR and cluster S_ℓ |
| $\xi_{\ell,i}^T(t), \xi_{\ell,i}^R(t)$ | distances between UAV/MR and S_ℓ via the i -th ray |
| $\alpha_{\text{RIS}}^T(t), \beta_{\text{RIS}}^T(t)$ | AAoD and EAoD from UAV to RIS |
| $\alpha_{\text{RIS}}^R(t), \beta_{\text{RIS}}^R(t)$ | AAoA and EAoA from RIS to MR |
| $\alpha_\ell^T(t), \beta_\ell^T(t)$ | AAoD and EAoD from UAV to S_ℓ |
| $\alpha_{\ell,i}^T(t), \beta_{\ell,i}^T(t)$ | AAoD and EAoD from UAV to S_ℓ via the i -th ray |
| $\alpha_\ell^R(t), \beta_\ell^R(t)$ | AAoA and EAoA from S_ℓ to MR |
| $\alpha_{\ell,i}^R(t), \beta_{\ell,i}^R(t)$ | AAoA and EAoA from S_ℓ to MR via the i -th ray |
| v_T, γ_T, η_T | moving speed and azimuth/elevation directions of UAV |
| v_R, γ_R | moving speed and azimuth direction of MR |
| θ_I, ϵ_I | vertical and horizontal rotation angles of RIS |
| $\alpha_{\text{in}}(t), \beta_{\text{in}}(t)$ | azimuth and normal incident angles from UAV to RIS |
| $\alpha_{\text{out}}(t), \beta_{\text{out}}(t)$ | azimuth and normal reflected angles from RIS to MR |

TABLE I
SUMMARY OF KEY PARAMETERS DEFINITIONS

however, is out of the scope of this paper and will be considered as a future work.

It has been shown in [26] that the channel shows sparsity in high frequency communications, especially for mmWave bands, which indicates that the received signal power concentrates on several main directions with relatively small angular spread when arriving at the MR. Therefore, we adopt the cluster structure to model the multipath scattering environments between the UAV and ground MR, where each cluster consisting of many scatterers accounts for a distinguishable path with resolvable delay, while the scatterers in the same cluster share similar distances as well as angles and hence result in indistinguishable rays with unresolvable delays [22]. In the proposed channel model, we assume that there exist L clusters with resolvable delays, in which the ℓ -th ($\ell = 1, 2, \dots, L$) cluster is denoted by S_ℓ . The definitions of the key model parameters are depicted in Fig. 3 and summarized in Table I. For the signal component from UAV to MR through RIS, the RIS will manipulate the waves by attaching an additional amplitude $\chi_{mn}(t)$ and phase $\varphi_{mn}(t)$ during the interaction. This process is similar to the signal being scattered by the scatterers; however, the major difference is that the reflection coefficient of the RIS unit is programmable and deterministic, while that of the scatterers is random. In light of this, we model the RIS by a *virtual cluster* and the RIS units by *virtual scatterers*, which means the rays reflected by different RIS units have similar propagation distances as well as angles and hence are indistinct. Considering that the UAV and RIS are generally deployed at a relatively higher altitude to provide a broader coverage, and the RIS has the ability to perform passive

beamforming, we only take into account the LoS propagation between RIS and UAV/MR.

A. Power Scaling Factor of the RIS Component

To study the power delivering capability of RIS, we assume that the UAV antenna array perform beamforming and the MR antenna array perform combing, respectively, so that the transmit and receive ULAs can be both regarded as point sources at the RIS side. We describe the power delivering capability of RIS by power scaling factor $\Omega_{\text{RIS}}(t)$, which is defined as the power gain of RIS propagation component relative to the same-distance free path and will be further used to derive the channel response in Section II.B. Then, we derive Theorem 1.

Theorem 1. *In RIS auxiliary UAV communications, the power scaling factor is given by*

$$\Omega_{\text{RIS}}(t) = \frac{d_M d_N \cos \beta_{\text{in}}(t) (\xi_{\text{RIS}}^T(t) + \xi_{\text{RIS}}^R(t))^2}{4\pi} \left| \sum_{m=1}^M \sum_{n=1}^N \frac{\chi_{mn}(t) e^{j(\varphi_{mn}(t) - \varphi_{mn}^{\text{dis}}(t))}}{\xi_{mn}^T(t) \xi_{mn}^R(t)} \right|^2, \quad (1)$$

where $\varphi_{mn}^{\text{dis}}(t)$ is the distance-related phase term through the (m, n) -th unit, and $\beta_{\text{in}}(t) \in [0, \frac{\pi}{2})$ is the incident angle to the normal direction of RIS.

Proof: See Appendix A for details. ■

It is worth mentioning that Theorem 1 presents the power scaling factor of RIS component at arbitrary reflection phase configuration, which implies how the power delivering capability of RIS is affected by the model parameters. Furthermore, it reveals that the incident angle $\beta_{\text{in}}(t)$ has a great impact on the received power, which has not been explicitly studied in the existing literature. Generally, a smaller incident angle corresponds to a larger reflection aperture, thus more power is reflected and forwarded to the MR. The received signal power can be significantly enhanced when the phases of the received waves from different RIS units are aligned, which can be achieved by performing passive beamforming at the RIS. Then, we have Corollary 1.

Corollary 1. *The optimal reflection phase of the (m, n) -th RIS unit for achieving a perfect beam aligning towards the MR under non-stationary propagation channels is given by*

$$\begin{aligned} \varphi_{mn}^{\text{opt}}(t) = & -\frac{2\pi}{\lambda} k_m d_M (\sin \beta_{\text{in}}(t) \cos \alpha_{\text{in}}(t) + \sin \beta_{\text{out}}(t) \cos \alpha_{\text{out}}(t)) \\ & - \frac{2\pi}{\lambda} k_n d_N (\sin \beta_{\text{in}}(t) \sin \alpha_{\text{in}}(t) + \sin \beta_{\text{out}}(t) \sin \alpha_{\text{out}}(t)) + \varphi_{\text{RIS}}, \end{aligned} \quad (2)$$

where φ_{RIS} is a controllable phase term that is independent of indexes m and n .

Proof: With the generalized law of reflection [27] and Theorem 1, Corollary 1 holds when $\varphi_{mn}(t)$ is configured to offset the phase difference of different units, i.e., $\varphi_{mn}^{\text{opt}}(t) = \varphi_{mn}^{\text{dis}}(t)$. ■

Corollary 1 indicates how the optimal reflection phases of RIS units are affected by the model parameters. Generally, φ_{RIS} can be set as zero for simplicity. When multiple RISs are deployed, however, φ_{RIS} in different RISs should be properly configured to ensure the signals from different RISs to be coherently superimposed at the MR. It is worth mentioning that the power scaling factor $\Omega_{\text{RIS}}(t)$ in (1) and optimal reflection phase $\varphi_{mn}^{\text{opt}}(t)$ in (2) are both time-varying due to the motion of UAV and MR, which is distinguished from conventional models with constant values. A more detailed discussion on the value of $\varphi_{mn}(t)$ will be presented in Section IV.

Alternatively, without considering time evolution, we assume that the material-related loss can be neglected, i.e., $\chi_{mn} = 1$, and assume that RIS reflection phase can be continuously and perfectly programmed, that is, $\varphi_{mn} = \varphi_{mn}^{\text{opt}}$. By approximating ξ_{mn}^T and ξ_{mn}^R with ξ_{RIS}^T and ξ_{RIS}^R , respectively, we express the power scaling factor under optimal reflection phase configuration as

$$\Omega_{\text{RIS}}^{\text{opt}} \approx \frac{M^2 N^2 d_M d_N \cos \beta_{\text{in}} (\xi_{\text{RIS}}^T + \xi_{\text{RIS}}^R)^2}{4\pi \xi_{\text{RIS}}^{T^2} \xi_{\text{RIS}}^{R^2}}. \quad (3)$$

Formula (3) indicates that the $\Omega_{\text{RIS}}^{\text{opt}}$ follows a squaring law with respect to the total number of RIS units MN , which meets with the results in [28]. Moreover, (3) implies that the relative distance between RIS and UAV/MR can also affect the received power even when the total propagation distance $\xi_{\text{RIS}}^T + \xi_{\text{RIS}}^R$ is fixed. Let $\xi_{\text{RIS}}^{TR} = \xi_{\text{RIS}}^T + \xi_{\text{RIS}}^R$ and $f(\xi_{\text{RIS}}^T) = \frac{\xi_{\text{RIS}}^{TR^2}}{(\xi_{\text{RIS}}^{TR} - \xi_{\text{RIS}}^T)^2 \xi_{\text{RIS}}^{T^2}}$, by taking the first order derivative with respect to ξ_{RIS}^T , we can show that $f(\xi_{\text{RIS}}^T)$ is concave and its minimum value occurs at $\xi_{\text{RIS}}^T = \xi_{\text{RIS}}^{TR}/2$. That is to say, we generally prefer to deploy the RIS closer to the UAV or MR instead of at the medium position so as to gain a larger received power. Overall, (3) embodies a useful guideline on the practical design and deployment of RIS to achieve higher power gains. Generally, more units, larger unit size, smaller incident angle, shorter end-to-end propagation distance, and closer location to the terminals can be more helpful.

B. Complex CIR of the Proposed Channel Model

The complex channel impulse response (CIR) of the proposed channel model can be characterized by a matrix of size $M_R \times M_T$, that is, $\mathbf{H}(t, \tau, \boldsymbol{\Theta}_T, \boldsymbol{\Theta}_R) = [h_{pq}(t, \tau, \boldsymbol{\Theta}_T, \boldsymbol{\Theta}_R)]_{M_R \times M_T}$, where t indicates moving time, τ stands for the propagation delay, and $\boldsymbol{\Theta}_T$ and $\boldsymbol{\Theta}_R$ denote the departure angle (azimuth angle of departure (AAoD) and elevation angle of departure (EAoD))

and arrival angle (azimuth angle of arrival (AAoA) and elevation angle of arrival (EAoA)) pair of the path, respectively. The $h_{pq}(t, \tau, \Theta_T, \Theta_R)$ denotes the complex CIR between the $(p \rightarrow q)$ -th transmit-receive antenna pair, which can be expressed as [26]

$$\begin{aligned} h_{pq}(t, \tau, \Theta_T, \Theta_R) &= h_{pq}^{\text{RIS}}(t) \delta(\tau - \tau_{\text{RIS}}(t)) \delta(\Theta_T - \Theta_T(\alpha_{\text{RIS}}^T(t), \beta_{\text{RIS}}^T(t))) \delta(\Theta_R - \Theta_R(\alpha_{\text{RIS}}^R(t), \beta_{\text{RIS}}^R(t))) \\ &+ \sum_{\ell=1}^L h_{\ell,pq}(t) \delta(\tau - \tau_{\ell}(t)) \delta(\Theta_T - \Theta_T(\alpha_{\ell}^T(t), \beta_{\ell}^T(t))) \delta(\Theta_R - \Theta_R(\alpha_{\ell}^R(t), \beta_{\ell}^R(t))), \quad (4) \end{aligned}$$

where $\tau_{\text{RIS}}(t) = (\xi_{\text{RIS}}^T(t) + \xi_{\text{RIS}}^R(t))/c$ denotes the propagation delay from UAV to MR through RIS, $\tau_{\ell}(t) = (\xi_{\ell}^T(t) + \xi_{\ell}^R(t))/c$ is the propagation delay from UAV to MR via cluster S_{ℓ} , and $c = 3.0 \times 10^8$ m/s is the speed of light. It is worth mentioning that the angle pair Θ_T and Θ_R in (4) are expressed in $\delta(\cdot)$ functions indicating that the channel response only exists in specific departure $\Theta_T(\alpha_{\text{RIS}|\ell}^T(t), \beta_{\text{RIS}|\ell}^T(t))$ and arrival $\Theta_R(\alpha_{\text{RIS}|\ell}^R(t), \beta_{\text{RIS}|\ell}^R(t))$ angle pairs, which characterize the sparsity of the mmWave channels [26]. Furthermore, $h_{pq}^{\text{RIS}}(t)$ and $h_{\ell,pq}(t)$ denote the channel coefficients of the RIS component and NLoS component via cluster S_{ℓ} , respectively. We consider an end-to-end expression of $h_{pq}^{\text{RIS}}(t)$ by incorporating the RIS power scaling factor, which is different from the existing works that interpret $h_{pq}^{\text{RIS}}(t)$ into two cascaded sub-channels [19]- [21]. Therefore, $h_{pq}^{\text{RIS}}(t)$ and $h_{\ell,pq}(t)$ can be respectively expressed as

$$\begin{aligned} h_{pq}^{\text{RIS}}(t) &= \sqrt{\frac{\Omega_{\text{RIS}}^{\text{opt}}(t)}{M^2 N^2}} \sum_{m=1}^M \sum_{n=1}^N \chi_{mn}(t) e^{j(\varphi_{mn}(t) - \frac{2\pi}{\lambda}(\xi_{\text{RIS}}^T(t) + \xi_{\text{RIS}}^R(t)))} \\ &\times e^{j\frac{2\pi}{\lambda}k_p\delta_T(\cos(\alpha_{\text{RIS}}^T(t) - \psi_T) \cos \beta_{\text{RIS}}^T(t) \cos \phi_T + \sin \beta_{\text{RIS}}^T(t) \sin \phi_T)} \\ &\times e^{j\frac{2\pi}{\lambda}k_q\delta_R(\cos(\alpha_{\text{RIS}}^R(t) - \psi_R) \cos \beta_{\text{RIS}}^R(t) \cos \phi_R + \sin \beta_{\text{RIS}}^R(t) \sin \phi_R)} \\ &\times e^{j\frac{2\pi}{\lambda}(k_m d_M(\sin \beta_{\text{in}}(t) \cos \alpha_{\text{in}}(t) + \sin \beta_{\text{out}}(t) \cos \alpha_{\text{out}}(t)) + k_n d_N(\sin \beta_{\text{in}}(t) \sin \alpha_{\text{in}}(t) + \sin \beta_{\text{out}}(t) \sin \alpha_{\text{out}}(t)))} \\ &\times e^{j\frac{2\pi}{\lambda}v_T t(\cos(\alpha_{\text{RIS}}^T(t) - \gamma_T) \cos \beta_{\text{RIS}}^T(t) \cos \eta_T + \sin \beta_{\text{RIS}}^T(t) \sin \eta_T)} e^{j\frac{2\pi}{\lambda}v_R t \cos(\alpha_{\text{RIS}}^R(t) - \gamma_R) \cos \beta_{\text{RIS}}^R(t)}, \quad (5) \\ h_{\ell,pq}(t) &= \sqrt{\frac{P_{\ell}(t)}{I}} \sum_{i=1}^I e^{j(\varphi_{\ell,i} - \frac{2\pi}{\lambda}(\xi_{\ell,i}^T(t) + \xi_{\ell,i}^R(t)))} \\ &\times e^{j\frac{2\pi}{\lambda}k_p\delta_T(\cos(\alpha_{\ell,i}^T(t) - \psi_T) \cos \beta_{\ell,i}^T(t) \cos \phi_T + \sin \beta_{\ell,i}^T(t) \sin \phi_T)} \end{aligned}$$

$$\begin{aligned} & \times e^{j\frac{2\pi}{\lambda}k_q\delta_R} \left(\cos(\alpha_{\ell,i}^R(t) - \psi_R) \cos \beta_{\ell,i}^R(t) \cos \phi_R + \sin \beta_{\ell,i}^R(t) \sin \phi_R \right) \\ & \times e^{j\frac{2\pi}{\lambda}v_T t} \left(\cos(\alpha_{\ell,i}^T(t) - \gamma_T) \cos \beta_{\ell,i}^T(t) \cos \eta_T + \sin \beta_{\ell,i}^T(t) \sin \eta_T \right) e^{j\frac{2\pi}{\lambda}v_R t \cos(\alpha_{\ell,i}^R(t) - \gamma_R) \cos \beta_{\ell,i}^R(t)}, \quad (6) \end{aligned}$$

where $k_p = \frac{M_T - 2p + 1}{2}$ and $k_q = \frac{M_R - 2q + 1}{2}$, λ is the wavelength, I is the number of rays in cluster S_ℓ , and $P_\ell(t)$ denotes the cluster power [24]. Moreover, $\{\varphi_{\ell,i}\}_{i=1,\dots,I}^{\ell=1,\dots,L}$ are assumed to be independent and uniformly distributed random phases, that is, $\varphi_{\ell,i} \sim \mathcal{U}[-\pi, \pi)$.

For the RIS component $h_{pq}^{\text{RIS}}(t)$, the initial distance/angular/delay parameters can be determined once the geometric setup among UAV, RIS, and MR is confirmed. For the cluster scattered components $h_{\ell,pq}(t)$, we assume that the initial distance/angular/delay parameters can be obtained from a measurement campaign or generated randomly [23], [26]. Then, the values of these aforementioned parameters at time t can be derived by exploiting the geometric relationships among the UAV, MR, and RIS/clusters based on the initial parameters and the moving speed-/directions/time of the UAV and MR. Therefore, the time-varying distances from the centers of the UAV and MR antenna arrays to the center of RIS can be respectively calculated as

$$\xi_{\text{RIS}}^T(t) = \sqrt{(x_I - r_T^x(t))^2 + (y_I - r_T^y(t))^2 + (z_I - H_0 - r_T^z(t))^2}, \quad (7)$$

$$\xi_{\text{RIS}}^R(t) = \sqrt{(x_I - \xi_R - r_R^x(t))^2 + (y_I - r_R^y(t))^2 + (z_I - r_R^z(t))^2}, \quad (8)$$

and the corresponding time-varying angles can be expressed as

$$\beta_{\text{RIS}}^R(t) = \arcsin \frac{z_I}{\xi_{\text{RIS}}^R(t)}, \quad (9)$$

$$\beta_{\text{RIS}}^T(t) = \arcsin \frac{z_I - H_0 - v_T t \sin \eta_T}{\xi_{\text{RIS}}^T(t)}, \quad (10)$$

$$\alpha_{\text{RIS}}^T(t) = \arccos \frac{x_I - v_T t \cos \eta_T \cos \gamma_T}{\sqrt{(x_I - r_T^x(t))^2 + (y_I - r_T^y(t))^2}}, \quad (11)$$

$$\alpha_{\text{RIS}}^R(t) = \arccos \frac{x_I - \xi_R - v_R t \cos \gamma_R}{\sqrt{(x_I - \xi_R - v_R t \cos \gamma_R)^2 + (y_I - v_R t \cos \gamma_R)^2}}. \quad (12)$$

Moreover, the time-varying distances from the centers of UAV and MR antenna arrays to cluster S_ℓ , denoted by $\xi_\ell^T(t)$ and $\xi_\ell^R(t)$, respectively, and those from the centers of UAV and MR antenna arrays to cluster S_ℓ via the i -th ray, they are, $\xi_{\ell,i}^T(t)$ and $\xi_{\ell,i}^R(t)$, respectively, can be calculated as

$$\xi_\ell^R(t) = \sqrt{(\xi_{R,\ell}^x(0) - r_R^x(t))^2 + (\xi_{R,\ell}^y(0) - r_R^y(t))^2 + (\xi_{R,\ell}^z(0) - r_R^z(t))^2}, \quad (13)$$

$$\xi_{\ell,i}^R(t) = \sqrt{(\xi_{R,\ell,i}^x(0) - r_R^x(t))^2 + (\xi_{R,\ell,i}^y(0) - r_R^y(t))^2 + (\xi_{R,\ell,i}^z(0) - r_R^z(t))^2}, \quad (14)$$

$$\xi_\ell^T(t) = \sqrt{(\xi_R + \xi_{R,\ell}^x(0) - r_T^x(t))^2 + (\xi_{R,\ell}^y(0) - r_T^y(t))^2 + (\xi_{R,\ell}^z(0) - H_0 - r_T^z(t))^2}, \quad (15)$$

$$\xi_{\ell,i}^T(t) = \sqrt{(\xi_R + \xi_{R,\ell,i}^x(0) - r_T^x(t))^2 + (\xi_{R,\ell,i}^y(0) - r_T^y(t))^2 + (\xi_{R,\ell,i}^z(0) - H_0 - r_T^z(t))^2}, \quad (16)$$

and the corresponding time-varying ray angles can be expressed as

$$\beta_{\ell,i}^R(t) = \arcsin \frac{\xi_\ell^R(0) \sin \beta_{\ell,i}^R(0)}{\xi_{\ell,i}^R(t)}, \quad (17)$$

$$\beta_{\ell,i}^T(t) = \arcsin \frac{\xi_\ell^R(0) \sin \beta_{\ell,i}^R(0) - H_0 - v_T t \cos \eta_T \cos \gamma_T}{\xi_{\ell,i}^T(t)}, \quad (18)$$

$$\alpha_{\ell,i}^R(t) = \arccos \frac{\xi_\ell^R(0) \cos \alpha_{\ell,i}^R(0) \cos \beta_{\ell,i}^R(0) - v_R t \cos \gamma_R}{\sqrt{(\xi_{R,\ell,i}^x(0) - r_R^x(t))^2 + (\xi_{R,\ell,i}^y(0) - r_R^y(t))^2}}, \quad (19)$$

$$\alpha_{\ell,i}^T(t) = \arccos \frac{\xi_R + \xi_\ell^R(0) \cos \alpha_{\ell,i}^R(0) \cos \beta_{\ell,i}^R(0) - v_T t \cos \eta_T \cos \gamma_T}{\sqrt{(\xi_R + \xi_{R,\ell,i}^x(0) - r_T^x(t))^2 + (\xi_{R,\ell,i}^y(0) - r_T^y(t))^2}}, \quad (20)$$

where we apply $t = 0$ to denote the initial values of these parameters. Moreover, $r_T^x(t) = v_T t \cos \eta_T \cos \gamma_T$, $r_T^y(t) = v_T t \cos \eta_T \sin \gamma_T$, and $r_T^z(t) = v_T t \sin \eta_T$ are the moving displacements of the UAV in the x , y , and z directions, respectively; while at the MR, they are expressed as $r_R^x(t) = v_R t \cos \gamma_R$, $r_R^y(t) = v_R t \sin \gamma_R$, and $r_R^z(t) = 0$, respectively. In addition, $\xi_{R,\ell}^x(0) = \xi_\ell^R(0) \cos \beta_\ell^R(0) \cos \alpha_\ell^R(0)$, $\xi_{R,\ell}^y(0) = \xi_\ell^R(0) \cos \beta_\ell^R(0) \sin \alpha_\ell^R(0)$, and $\xi_{R,\ell}^z(0) = \xi_\ell^R(0) \sin \beta_\ell^R(0)$ constitute the initial distance vector from MR to cluster S_ℓ , that is, $[\xi_{R,\ell}^x(0), \xi_{R,\ell}^y(0), \xi_{R,\ell}^z(0)]^T$; meanwhile, $[\xi_{R,\ell,i}^x(0), \xi_{R,\ell,i}^y(0), \xi_{R,\ell,i}^z(0)]^T$ denotes the distance vector from MR to cluster S_ℓ via the i -th ray, where $\xi_{R,\ell,i}^x(0) = \xi_\ell^R(0) \cos \beta_{\ell,i}^R(0) \cos \alpha_{\ell,i}^R(0)$, $\xi_{R,\ell,i}^y(0) = \xi_\ell^R(0) \cos \beta_{\ell,i}^R(0) \sin \alpha_{\ell,i}^R(0)$, and $\xi_{R,\ell,i}^z(0) = \xi_\ell^R(0) \sin \beta_{\ell,i}^R(0)$. The derivations of the incident $(\alpha_{\text{in}}(t), \beta_{\text{in}}(t))$ and reflected $(\alpha_{\text{out}}(t), \beta_{\text{out}}(t))$ angles are in Appendix B.

Moreover, the time-varying cluster power $P_\ell(t)$ is generated by [24]

$$P_\ell(t) = \exp \left(-\tau_\ell(t) \frac{r_\tau - 1}{r_\tau \sigma_\tau} \right) \cdot 10^{\frac{-Z_\ell}{10}}, \quad (21)$$

where r_τ is the delay scaling parameter, σ_τ is the delay spread, and Z_ℓ is a Gaussian distributed random variable, i.e., $Z_\ell \sim \mathcal{N}(0, \zeta^2)$, and their values can be obtained from Table 7.5.6 in [24].

Corollary 2. *When the physical direct path between UAV and MR is obstructed, the fading of the end-to-end channel $h_{pq}(t, \tau, \Theta_T, \Theta_R)$ in (4) can be characterized by Rician fading. Moreover, by borrowing the concept of Rice factor from Rician fading channels, we define the virtual Rice factor of the proposed non-stationary RIS auxiliary UAV mmWave channel model as*

$$K^{\text{vir}}(t) = \frac{\Omega_{\text{RIS}}(t)}{\sum_{\ell=1}^L P_{\ell}(t)}. \quad (22)$$

Proof: See Appendix C for details. ■

Corollary 2 reveals that the physical indirect RIS component $h_{pq}^{\text{RIS}}(t)$ has the ability to provide a deterministic component on the received signals, which behaves similarly to the physical direct LoS component between the UAV and MR, thus we name it the *virtual LoS (V-LoS)* component provided by RIS. Moreover, Corollary 2 provides a new view on the modeling of the channel statistics in RIS auxiliary communication systems by considering the end-to-end propagation channel between the transceiver, which is distinguishable from the results in [19]- [21].

In this paper, we mainly focus on the small-scale fading characterization of the RIS auxiliary MIMO UAV communication channels in mmWave bands. We normalize the power of the complex CIR $h_{pq}(t, \tau, \Theta_T, \Theta_R)$ to one, to provide a general representation, as [29]

$$\begin{aligned} h_{pq}^{\text{RIS}}(t) = & \sqrt{\frac{K^{\text{vir}}(t)}{(K^{\text{vir}}(t) + 1)|\Upsilon(t)|^2}} \sum_{m=1}^M \sum_{n=1}^N \chi_{mn}(t) e^{j\left(\varphi_{mn}(t) - \frac{2\pi}{\lambda}(\xi_{\text{RIS}}^T(t) + \xi_{\text{RIS}}^R(t))\right)} \\ & \times e^{j\frac{2\pi}{\lambda}k_p\delta_T \left(\cos(\alpha_{\text{RIS}}^T(t) - \psi_T) \cos\beta_{\text{RIS}}^T(t) \cos\phi_T + \sin\beta_{\text{RIS}}^T(t) \sin\phi_T\right)} \\ & \times e^{j\frac{2\pi}{\lambda}k_q\delta_R \left(\cos(\alpha_{\text{RIS}}^R(t) - \psi_R) \cos\beta_{\text{RIS}}^R(t) \cos\phi_R + \sin\beta_{\text{RIS}}^R(t) \sin\phi_R\right)} \\ & \times e^{j\frac{2\pi}{\lambda} \left(k_m d_M (\sin\beta_{\text{in}}(t) \cos\alpha_{\text{in}}(t) + \sin\beta_{\text{out}}(t) \cos\alpha_{\text{out}}(t)) + k_n d_N (\sin\beta_{\text{in}}(t) \sin\alpha_{\text{in}}(t) + \sin\beta_{\text{out}}(t) \sin\alpha_{\text{out}}(t))\right)} \\ & \times e^{j\frac{2\pi}{\lambda}v_T t \left(\cos(\alpha_{\text{RIS}}^T(t) - \gamma_T) \cos\beta_{\text{RIS}}^T(t) \cos\eta_T + \sin\beta_{\text{RIS}}^T(t) \sin\eta_T\right)} e^{j\frac{2\pi}{\lambda}v_R t \cos(\alpha_{\text{RIS}}^R(t) - \gamma_R) \cos\beta_{\text{RIS}}^R(t)}, \quad (23) \end{aligned}$$

$$\begin{aligned} h_{\ell,pq}(t) = & \sqrt{\frac{P'_{\ell}(t)}{(K^{\text{vir}}(t) + 1)I}} \sum_{i=1}^I e^{j\left(\varphi_{\ell,i} - \frac{2\pi}{\lambda}(\xi_{\ell,i}^T(t) + \xi_{\ell,i}^R(t))\right)} \\ & \times e^{j\frac{2\pi}{\lambda}k_p\delta_T \left(\cos(\alpha_{\ell,i}^T(t) - \psi_T) \cos\beta_{\ell,i}^T(t) \cos\phi_T + \sin\beta_{\ell,i}^T(t) \sin\phi_T\right)} \\ & \times e^{j\frac{2\pi}{\lambda}k_q\delta_R \left(\cos(\alpha_{\ell,i}^R(t) - \psi_R) \cos\beta_{\ell,i}^R(t) \cos\phi_R + \sin\beta_{\ell,i}^R(t) \sin\phi_R\right)} \\ & \times e^{j\frac{2\pi}{\lambda}v_T t \left(\cos(\alpha_{\ell,i}^T(t) - \gamma_T) \cos\beta_{\ell,i}^T(t) \cos\eta_T + \sin\beta_{\ell,i}^T(t) \sin\eta_T\right)} e^{j\frac{2\pi}{\lambda}v_R t \cos(\alpha_{\ell,i}^R(t) - \gamma_R) \cos\beta_{\ell,i}^R(t)}, \quad (24) \end{aligned}$$

where $\Upsilon(t) = \sum_{m=1}^M \sum_{n=1}^N \chi_{mn}(t) e^{j(\varphi_{mn}(t) - \varphi_{mn}^{dis}(t))}$. The $P'_\ell(t) = P_\ell(t) / \sum_{\ell=1}^L P_\ell(t)$ is the normalized power ratio of the clusters [24]. Note that $\varphi_{mn}(t)$ in (23) stands for the programmable RIS reflection phase, whose optimal value can be obtained from Corollary 1. Consequently, formulas (23) and (24) provide a generalized description of the end-to-end physical properties of RIS auxiliary UAV-to-ground mmWave communication channels, which has the ability to effectively reveal the programmable property of the channels owing to the presence of RIS, thus is distinguishable from the conventional cascaded channel models in [19]- [21]. Alternatively, when we ignore the time evolution of the model parameters, the proposed channel model can be used to describe stationary channels; when we set cluster number L as one, the proposed channel model can be used to describe narrowband channels; and when we set the RIS component $h_{pq}^{\text{RIS}}(t)$ as zero, the proposed channel model reduce to be conventional Rayleigh fading channels without RIS. This shows the generality of the proposed channel model.

III. STATISTICAL PROPERTIES OF THE PROPOSED CHANNEL MODEL

A. Fading Characteristic

In conventional no-RIS auxiliary UAV mmWave communication system, the fading of the end-to-end propagation channel between the transceiver is characterized by Rayleigh fading when the direct path is blocked. This can be derived from the proposed channel model by setting the RIS component $h_{pq}^{\text{RIS}}(t)$ in (4) as zero. Then, by introducing a RIS between the UAV and MR, Corollary 2 has shown that the fading of the proposed RIS auxiliary channel can be characterized by Rician fading with virtual Rice factor $K^{\text{vir}}(t)$ and envelope power $\Omega_{\text{RIS}}(t) + \sum_{\ell=1}^L P_\ell(t)$.

It is worth mentioning that when the RIS apply the random reflection phase controlling mechanism in each unit, the reflection phase $\varphi_{mn}(t)$ becomes a random variable, and hence the RIS component $h_{pq}^{\text{RIS}}(t)$ becomes a random process. In this case, the fading of the end-to-end RIS auxiliary channel depends on the reflection phase controlling mechanism as well as the total unit number, and cannot be characterized by Rician fading. An example is that when the RIS apply random uniform reflection phase control, that is, $\varphi_{mn}(t) \sim \mathcal{U}[-\pi, \pi)$, and the unit number MN is large enough, $h_{pq}(t, \tau, \Theta_T, \Theta_R)$ can be characterized by Rayleigh fading with envelope power $\mathbb{E}[\Omega_{\text{RIS}}(t)] + \sum_{\ell=1}^L P_\ell(t)$ based on the Central Limit Theorem.

B. Time-varying Spatial-Temporal (ST) Cross-Correlation Function (CCF)

As shown in [23], [30], the local correlation properties of a channel are determined by the correlation properties between $h_{pq}(t)$ and $h_{p'q'}(t + \Delta t)$ in each tap; meanwhile, it is generally assumed that there is no correlation between different clusters. Therefore, the normalized time-varying ST CCF of the proposed channel model can be defined as [23]

$$\rho_{(p,q),(p',q')}(t, \Delta p, \Delta q, \Delta t) = \frac{\mathbb{E}[h_{pq}^*(t)h_{p'q'}(t + \Delta t)]}{\sqrt{\mathbb{E}[|h_{pq}(t)|^2]\mathbb{E}[|h_{p'q'}(t + \Delta t)|^2]}}, \quad (25)$$

where Δt is the time difference, $\Delta p = |k_{p'} - k_p|\delta_T/\lambda$ and $\Delta q = |k_{q'} - k_q|\delta_R/\lambda$ denote the normalized antenna spacings of the UAV and MR antenna arrays, respectively, where $p, p', q,$ and q' are the antenna indexes. In addition, $h_{pq}(t)$ and $h_{p'q'}(t + \Delta t)$ denote the complex channel coefficients of the $(p \rightarrow q)$ -th and $(p' \rightarrow q')$ -th transmit-receive antenna pairs, respectively.

By substituting (23) and (24) into (25), we obtain the time-varying ST CCF of the proposed channel model as $\rho_{(p,q),(p',q')}(t, \Delta p, \Delta q, \Delta t) = \rho_{(p,q),(p',q')}^{\text{RIS}}(t, \Delta p, \Delta q, \Delta t) + \rho_{(p,q),(p',q'),\ell}^{\text{NLoS}}(t, \Delta p, \Delta q, \Delta t)$, in which the $\rho_{(p,q),(p',q')}^{\text{RIS}}(t, \Delta p, \Delta q, \Delta t)$ and $\rho_{(p,q),(p',q'),\ell}^{\text{NLoS}}(t, \Delta p, \Delta q, \Delta t)$ denote the local ST CCF of the RIS and NLoS components, respectively. Moreover, by further imposing $\Delta t = 0$, we can obtain the following spatial CCF of the RIS component

$$\begin{aligned} \rho_{(p,q),(p',q')}^{\text{RIS}}(t, \Delta p, \Delta q) &= \frac{K^{\text{vir}}(t)}{K^{\text{vir}}(t) + 1} \\ &\times e^{j2\pi\Delta p \left(\cos(\alpha_{\text{RIS}}^T(t) - \psi_T) \cos \beta_{\text{RIS}}^T(t) \cos \phi_T + \sin \beta_{\text{RIS}}^T(t) \sin \phi_T \right)} \\ &\times e^{j2\pi\Delta q \left(\cos(\alpha_{\text{RIS}}^R(t) - \psi_R) \cos \beta_{\text{RIS}}^R(t) \cos \phi_R + \sin \beta_{\text{RIS}}^R(t) \sin \phi_R \right)}, \end{aligned} \quad (26)$$

and the spatial CCF of the NLoS components

$$\begin{aligned} \rho_{(p,q),(p',q'),\ell}^{\text{NLoS}}(t, \Delta p, \Delta q) &= \frac{P'_\ell(t)}{K^{\text{vir}}(t) + 1} \\ &\times \int_{-\pi}^{\pi} \int_{-\pi}^{\pi} e^{j2\pi\Delta p \left(\cos(\alpha_\ell^T(t) - \psi_T) \cos \beta_\ell^T(t) \cos \phi_T + \sin \beta_\ell^T(t) \sin \phi_T \right)} \\ &\times e^{j2\pi\Delta q \left(\cos(\alpha_\ell^R(t) - \psi_R) \cos \beta_\ell^R(t) \cos \phi_R + \sin \beta_\ell^R(t) \sin \phi_R \right)} f(\alpha_\ell^R, \beta_\ell^R) d(\alpha_\ell^R, \beta_\ell^R), \end{aligned} \quad (27)$$

where $f(\alpha_\ell^R, \beta_\ell^R)$ is the joint probability density function (PDF) of the received azimuth α_ℓ^R and elevation β_ℓ^R angles from cluster S_ℓ . In general, the arrival angles (AAoA and EAoA) and departure angles (AAoD and EAoD) of the waves are dependent on each other when the

geometrical setup is confirmed in the proposed single-bounced channel model [23]. It should be noted that in cluster structure, the directions of the rays in each cluster are limited to a certain range. It is reasonable to adopt the truncated Gaussian PDF to characterize the angular distribution, hence the PDF for the wave with direction ϑ being limited within the interval from ϑ_{low} to ϑ_{up} , i.e., $\vartheta \in [\vartheta_{\text{low}}, \vartheta_{\text{up}}]$, can be expressed as

$$f(\vartheta, \mu_\vartheta, \sigma_\vartheta, \vartheta_{\text{low}}, \vartheta_{\text{up}}) = \frac{\frac{1}{\sigma_\vartheta} u\left(\frac{\vartheta - \mu_\vartheta}{\sigma_\vartheta}\right)}{\Phi\left(\frac{\vartheta_{\text{up}} - \mu_\vartheta}{\sigma_\vartheta}\right) - \Phi\left(\frac{\vartheta_{\text{low}} - \mu_\vartheta}{\sigma_\vartheta}\right)}, \quad (28)$$

where μ_ϑ and σ_ϑ denote the mean value and angle spread of the signal direction ϑ , respectively. In addition, $u(\varsigma)$ is the PDF of the standard normal distributed random variable ς , which can be expressed as $u(\varsigma) = \frac{1}{\sqrt{2\pi}} \exp\{-\frac{\varsigma^2}{2}\}$, whereas $\Phi(\varsigma) = \int_{-\infty}^{\varsigma} u(\varsigma') d\varsigma' = \frac{1}{2} (1 + \text{erf}(\frac{\varsigma}{\sqrt{2}}))$ represents the cumulative distribution function (CDF) of the standard normal distributed random variable ς with $\text{erf}(\cdot)$ being the Gauss error function. The signal azimuth and elevation angles are generally assumed to be independent of each other, thus the joint PDF in (27) can be derived from (28) as $f(\alpha_\ell^R, \beta_\ell^R) = f(\alpha_\ell^R, \mu_{\alpha_\ell^R}, \sigma_{\alpha_\ell^R}, \alpha_{\ell, \text{low}}^R, \alpha_{\ell, \text{up}}^R) \cdot f(\beta_\ell^R, \mu_{\beta_\ell^R}, \sigma_{\beta_\ell^R}, \beta_{\ell, \text{low}}^R, \beta_{\ell, \text{up}}^R)$.

C. Temporal Auto-Correlation Function (ACF) and Doppler Power Spectral Density (PSD)

The temporal ACF of the proposed channel model can be derived from the ST CCF $\rho_{(p,q),(p',q')}(t, \Delta p, \Delta q, \Delta t)$ by applying $\Delta p = \Delta q = 0$, that is, $p = p'$ and $q = q'$, which is expressed as

$$\rho(t, \Delta t) = \rho^{\text{RIS}}(t, \Delta t) + \rho_\ell^{\text{NLoS}}(t, \Delta t), \quad (29)$$

where $\rho^{\text{RIS}}(t, \Delta t)$ and $\rho_\ell^{\text{NLoS}}(t, \Delta t)$ stand for the temporal ACFs of the RIS and NLoS components, respectively, which are expressed as

$$\begin{aligned} \rho^{\text{RIS}}(t, \Delta t) &= \sqrt{\frac{K^{\text{vir}}(t)}{K^{\text{vir}}(t) + 1}} \sqrt{\frac{K^{\text{vir}}(t + \Delta t)}{K^{\text{vir}}(t + \Delta t) + 1}} \times \frac{\mathbb{E}[\Upsilon^*(t) \Upsilon(t + \Delta t)]}{\sqrt{\mathbb{E}[|\Upsilon(t)|^2] \mathbb{E}[|\Upsilon(t + \Delta t)|^2]}} \\ &\times e^{j \frac{2\pi}{\lambda} (\xi_{\text{RIS}}^T(t) - \xi_{\text{RIS}}^T(t + \Delta t) + \xi_{\text{RIS}}^R(t) - \xi_{\text{RIS}}^R(t + \Delta t))} \\ &\times e^{-j \frac{2\pi}{\lambda} k_p \delta_T \left(\cos(\alpha_{\text{RIS}}^T(t) - \psi_T) \cos \beta_{\text{RIS}}^T(t) \cos \phi_T + \sin \beta_{\text{RIS}}^T(t) \sin \phi_T \right)} \\ &\times e^{j \frac{2\pi}{\lambda} k_p \delta_T \left(\cos(\alpha_{\text{RIS}}^T(t + \Delta t) - \psi_T) \cos \beta_{\text{RIS}}^T(t + \Delta t) \cos \phi_T + \sin \beta_{\text{RIS}}^T(t + \Delta t) \sin \phi_T \right)} \\ &\times e^{-j \frac{2\pi}{\lambda} k_q \delta_R \left(\cos(\alpha_{\text{RIS}}^R(t) - \psi_R) \cos \beta_{\text{RIS}}^R(t) \cos \phi_R + \sin \beta_{\text{RIS}}^R(t) \sin \phi_R \right)} \\ &\times e^{j \frac{2\pi}{\lambda} k_q \delta_R \left(\cos(\alpha_{\text{RIS}}^R(t + \Delta t) - \psi_R) \cos \beta_{\text{RIS}}^R(t + \Delta t) \cos \phi_R + \sin \beta_{\text{RIS}}^R(t + \Delta t) \sin \phi_R \right)} \end{aligned}$$

$$\begin{aligned}
& \times e^{-j\frac{2\pi}{\lambda}v_T t} \left(\cos(\alpha_{\text{RIS}}^T(t) - \gamma_T) \cos \beta_{\text{RIS}}^T(t) \cos \eta_T + \sin \beta_{\text{RIS}}^T(t) \sin \eta_T \right) \\
& \times e^{j\frac{2\pi}{\lambda}v_T(t+\Delta t)} \left(\cos(\alpha_{\text{RIS}}^T(t+\Delta t) - \gamma_T) \cos \beta_{\text{RIS}}^T(t+\Delta t) \cos \eta_T + \sin \beta_{\text{RIS}}^T(t+\Delta t) \sin \eta_T \right) \\
& \times e^{j\frac{2\pi}{\lambda}(v_R(t+\Delta t) \cos(\alpha_{\text{RIS}}^R(t+\Delta t) - \gamma_R) \cos \beta_{\text{RIS}}^R(t+\Delta t) - v_R t \cos(\alpha_{\text{RIS}}^R(t) - \gamma_R) \cos \beta_{\text{RIS}}^R(t))}, \quad (30)
\end{aligned}$$

$$\begin{aligned}
\rho_{\ell}^{\text{NLoS}}(t, \Delta t) &= \sqrt{\frac{P'_{\ell}(t)}{K^{\text{vir}}(t) + 1}} \sqrt{\frac{P'_{\ell}(t + \Delta t)}{K^{\text{vir}}(t + \Delta t) + 1}} \\
&\times \frac{1}{I} \sum_{i=1}^I \mathbb{E} \left\{ e^{j\frac{2\pi}{\lambda}(\xi_{\ell,i}^T(t) - \xi_{\ell,i}^T(t+\Delta t) + \xi_{\ell,i}^R(t) - \xi_{\ell,i}^R(t+\Delta t))} \right. \\
&\times e^{-j\frac{2\pi}{\lambda}k_p \delta_T} \left(\cos(\alpha_{\ell,i}^T(t) - \psi_T) \cos \beta_{\ell,i}^T(t) \cos \phi_T + \sin \beta_{\ell,i}^T(t) \sin \phi_T \right) \\
&\times e^{j\frac{2\pi}{\lambda}k_p \delta_T} \left(\cos(\alpha_{\ell,i}^T(t+\Delta t) - \psi_T) \cos \beta_{\ell,i}^T(t+\Delta t) \cos \phi_T + \sin \beta_{\ell,i}^T(t+\Delta t) \sin \phi_T \right) \\
&\times e^{-j\frac{2\pi}{\lambda}k_q \delta_R} \left(\cos(\alpha_{\ell,i}^R(t) - \psi_R) \cos \beta_{\ell,i}^R(t) \cos \phi_R + \sin \beta_{\ell,i}^R(t) \sin \phi_R \right) \\
&\times e^{j\frac{2\pi}{\lambda}k_q \delta_R} \left(\cos(\alpha_{\ell,i}^R(t+\Delta t) - \psi_R) \cos \beta_{\ell,i}^R(t+\Delta t) \cos \phi_R + \sin \beta_{\ell,i}^R(t+\Delta t) \sin \phi_R \right) \\
&\times e^{j\frac{2\pi}{\lambda}v_T(t+\Delta t)} \left(\cos(\alpha_{\ell,i}^T(t+\Delta t) - \gamma_T) \cos \beta_{\ell,i}^T(t+\Delta t) \cos \eta_T + \sin \beta_{\ell,i}^T(t+\Delta t) \sin \eta_T \right) \\
&\times e^{-j\frac{2\pi}{\lambda}v_T t} \left(\cos(\alpha_{\ell,i}^T(t) - \gamma_T) \cos \beta_{\ell,i}^T(t) \cos \eta_T + \sin \beta_{\ell,i}^T(t) \sin \eta_T \right) \\
&\times e^{j\frac{2\pi}{\lambda}(v_R(t+\Delta t) \cos(\alpha_{\ell,i}^R(t+\Delta t) - \gamma_R) \cos \beta_{\ell,i}^R(t+\Delta t) - v_R t \cos(\alpha_{\ell,i}^R(t) - \gamma_R) \cos \beta_{\ell,i}^R(t))} \left. \right\}. \quad (31)
\end{aligned}$$

It is obvious that the temporal ACFs of the proposed channel model depend on time t and time difference Δt , which reveals the non-stationarity of the channel model. Moreover, (30) indicates that the RIS component has the ability to provide more favourable temporal correlation of the signals by appropriately programming the RIS reflection phases $\varphi_{mn}(t)$, to boost the communications.

The Doppler PSD of the proposed channel model is defined as the Fourier transform of temporal ACF $\rho(t, \Delta t)$ in (29) with respect to time difference Δt [25], that is,

$$S(t, \nu) = \int_{-\infty}^{\infty} \rho(t, \Delta t) e^{-j2\pi\nu\Delta t} d(\Delta t) = S^{\text{RIS}}(t, \nu) + S_{\ell}^{\text{NLoS}}(t, \nu), \quad (32)$$

where ν stands for the Doppler frequency, and $S^{\text{RIS}}(t, \nu)$ and $S_{\ell}^{\text{NLoS}}(t, \nu)$ denote the Doppler PSDs of the RIS and NLoS components, respectively, which are expressed as

$$S^{\text{RIS}}(t, \nu) = \int_{-\infty}^{\infty} \rho^{\text{RIS}}(t, \Delta t) e^{-j2\pi\nu\Delta t} d(\Delta t), \quad (33)$$

$$S_{\ell}^{\text{NLoS}}(t, \nu) = \int_{-\infty}^{\infty} \rho_{\ell}^{\text{NLoS}}(t, \Delta t) e^{-j2\pi\nu\Delta t} d(\Delta t). \quad (34)$$

It is obvious that the Doppler PSD of the proposed channel model is related to the moving time t as well as the moving states (speeds and directions) of the UAV and MR, which is in agreement with the models in [25].

D. Time-varying Frequency Correlation Function (FCF) and Power Delay Profile (PDP)

The time-varying transfer function of the proposed channel model is defined as the Fourier transform of the complex CIR $h_{pq}(t, \tau, \Theta_T, \Theta_R)$ in (4) with respect to the propagation delay τ , which is expressed as

$$H_{pq}(t, f) = h_{pq}^{\text{RIS}}(t) e^{-j2\pi f \tau^{\text{RIS}}(t)} + \sum_{\ell=1}^L h_{\ell, pq}(t) e^{-j2\pi f \tau_{\ell}(t)}. \quad (35)$$

Thus, the normalized FCF of the proposed channel model can be defined as [31]

$$\rho_{H_{pq}}(t, \Delta f) = \frac{\mathbb{E}[H_{pq}^*(t, f) H_{pq}(t, f + \Delta f)]}{\sqrt{\mathbb{E}[|H_{pq}(t, f)|^2] \mathbb{E}[|H_{pq}(t, f + \Delta f)|^2]}}, \quad (36)$$

where Δf denotes frequency separation. With the uncorrelated scattering (US) assumption [30], the substitution of (5), (6), and (35) into (36) yields the following FCF

$$\rho_{H_{pq}}(t, \Delta f) = \frac{K^{\text{vir}}(t)}{K^{\text{vir}}(t) + 1} e^{-j2\pi \Delta f \tau^{\text{RIS}}(t)} + \frac{1}{K^{\text{vir}}(t) + 1} \sum_{\ell=1}^L P'_{\ell}(t) e^{-j2\pi \Delta f \tau_{\ell}(t)}. \quad (37)$$

By applying inverse Fourier transform to the FCF $\rho_{H_{pq}}(t, \Delta f)$ with respect to frequency separation Δf , we can further derive the PDP of the proposed channel model as

$$S_{H_{pq}}(t, \tau) = \frac{K^{\text{vir}}(t)}{K^{\text{vir}}(t) + 1} \delta(\tau - \tau^{\text{RIS}}(t)) + \frac{1}{K^{\text{vir}}(t) + 1} \sum_{\ell=1}^L P'_{\ell}(t) \delta(\tau - \tau_{\ell}(t)). \quad (38)$$

It can be seen that the FCF and PDP of the proposed channel model are related to absolute time t but independent of frequency f , which indicates that the channel model is non-stationary in time domain but stationary in frequency domain. Moreover, the reflection phase controlling mechanism will also affect the FCF and PDP through the power scaling factor, which is a specific feature of the RIS auxiliary communication channels.

IV. RESULTS AND DISCUSSIONS

In this section, we numerically study the channel characteristics of the proposed channel model by comparing the theoretical results with simulated and measurement results.

A. Simulation Setup

The proposed channel model is operated at a carrier frequency of $f_c = 28$ GHz. The parameters used in the simulations are listed here or specified otherwise: $M_T = 4$, $M_R = 6$, $\xi_R = 100$ m, $H_0 = 50$ m, $\chi_{mn} = 1$, $\delta_T = \delta_R = \lambda/2$, $\psi_T = \pi/3$, $\phi_T = \pi/4$, $\psi_R = \pi/4$, $\phi_R = \pi/4$, $\xi_\ell^R(0) = 60$ m, $\mu_{\alpha_\ell^R} = 2\pi/3$, $\sigma_{\alpha_\ell^R} = \pi/18$, $\mu_{\beta_\ell^R} = \pi/4$, and $\sigma_{\alpha_\ell^R} = \pi/18$ [26], [31]. Two kinds of configurations of RIS with $MN = 4 \times 10^4$ are considered, that is, RIS_A with strip configuration $M = 400$, $N = 100$ and RIS_B with square configuration $M = N = 200$. The RIS is located at $(x_I, y_I, z_I) = (70 \text{ m}, 30 \text{ m}, 15 \text{ m})$ with the rotation angles $\theta_I = -\pi/18$ and $\epsilon_I = -\pi/18$, and the size of the RIS unit is set as $d_M = d_N = \lambda/4$. Finally, the moving speed and direction of the UAV are set as $v_T = 5$ m/s, $\gamma_T = 0$ in azimuth direction and $\eta_T = 0$ in elevation direction, respectively, whereas at MR they are set as $v_R = 2$ m/s and $\gamma_R = 0$.

Moreover, the impacts of different reflection phase controlling mechanisms are evaluated, where

i) *Optimal*: The RIS controller applies optimal reflection phase controlling mechanism with $\varphi_{mn}(t) = \varphi_{mn}^{\text{opt}}(t)$. Therefore, $\Omega_{\text{RIS}}(t) = \Omega_{\text{RIS}}^{\text{opt}}(t)$ and the channel is characterized by Rician fading.

ii) *Discrete*: The RIS controller applies discrete reflection phase controlling mechanism with $\varphi_{mn}(t) = \varphi_{mn}^{\text{discrete}}(t)$, where $\varphi_{mn}^{\text{discrete}}(t)$ is the discretization of $\varphi_{mn}^{\text{opt}}(t)$. In this case, $\Omega_{\text{RIS}}(t) = \Omega_{\text{RIS}}^{\text{opt}}(t)|\Upsilon(t)|^2/(M^2N^2)$ and the channel is characterized by Rician fading.

iii) *Constant*: The RIS controller applies constant reflection phase controlling mechanism with $\varphi_{mn}(t) = \varphi_{mn}^{\text{const}}$, where $\varphi_{mn}^{\text{const}}$ is the optimal reflection phase at the initial instant, that is, $\varphi_{mn}^{\text{const}} = \varphi_{mn}^{\text{opt}}(0)$. In this case, $\Omega_{\text{RIS}}(t) = \Omega_{\text{RIS}}^{\text{opt}}(t)|\Upsilon(t)|^2/(M^2N^2)$ and the proposed RIS-assisted channel model is characterized by Rician fading.

iv) *Random*: The RIS controller applies random reflection phase controlling mechanism with $\varphi_{mn}(t) \sim \mathcal{U}[-\pi, \pi)$. In this case, the proposed model is characterized by Rayleigh fading with $K^{\text{vir}}(t) = \Omega_{\text{RIS}}^{\text{opt}}(t)/(MN \sum_{\ell}^L P_{\ell}(t)(t))$ being the power ratio between RIS and NLoS component.

B. Performance Analysis

1) *Power Delivering Capability of RIS*: We first investigate the reflection phase of RIS under optimal reflection phase configuration based on (2). Figure 4 presents the normalized optimal reflection phase of different units in a 200×200 -unit square RIS array, that is, RIS_B, where the phase values are normalized by modulo dividing 2π . It can be seen that the normalized reflection phases show periodicity over the array at $t = 0$, which means different RIS units share the same

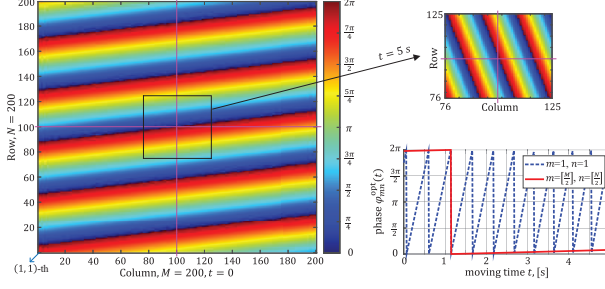


Fig. 4. Normalized reflection phases of RIS under optimal reflection phase configuration.

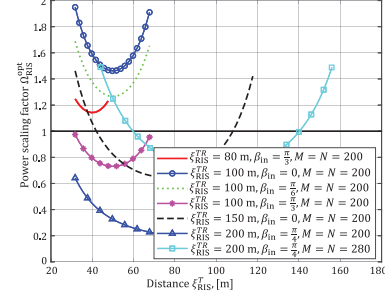


Fig. 5. Power scaling factor $\Omega_{\text{RIS}}^{\text{opt}}$ of the RIS component under optimal reflection phase configuration.

reflection phase in order to reflect the incident signals towards the target point. After a time interval of $t = 5$ s, the phase pattern changes, but the periodicity of phase values still holds. This means the RIS controller should update the reflection phases in a real-time manner to meet with the time-varying property of the channel. Moreover, Fig. 4 implies that the reflection phase of the central unit vary much more slowly as compared to that of the corner unit.

In Fig. 5, we study the power delivering capability of RIS under optimal phase configuration, which is characterized by the power scaling factor $\Omega_{\text{RIS}}^{\text{opt}}$ in this paper. It can be seen that the $\Omega_{\text{RIS}}^{\text{opt}}$ firstly decrease and then increase as distance ξ_{RIS}^T increases, where the inflexion occurs at $\xi_{\text{RIS}}^T = \xi_{\text{RIS}}^{TR}/2$. Moreover, the $\Omega_{\text{RIS}}^{\text{opt}}$ decreases when the propagation distance ξ_{RIS}^{TR} and normal incident angle β_{in} increase. When the propagation distance is small, such as $\xi_{\text{RIS}}^{TR} = 80$ and 100 m, the RIS has the ability to provide positive power gain ($\Omega_{\text{RIS}}^{\text{opt}} > 1$) than LoS path at arbitrary location even with a relatively large incident angle $\pi/3$ and $\pi/6$, respectively, thus motivates the usage of RIS in *short-range scenarios*, i.e., indoor scenario. Then, by comparing the curves with $\xi_{\text{RIS}}^{TR} = 200$ m, we find that some positive locations of RIS occurs when increasing the unit numbers. Overall, the results in Fig. 5 are consistent with the theoretical results in (3), which is helpful for the system implementation.

2) *Fading Characterization*: We investigate the fading characteristics of the proposed channel model in Fig. 6 under optimal and random reflection phase configurations. By comparing the simulated results with theoretical results, we can see that the proposed channel model tends to be characterized by Rician fading under optimal reflection phase configuration, whereas by Rayleigh fading under random reflection phase configuration. The proposed channel model also satisfies

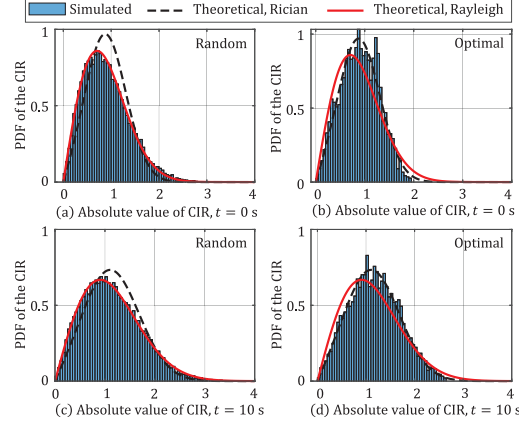


Fig. 6. Fading characteristics of the proposed RIS auxiliary channel model where $K^{\text{vir}}(0) = 1.5$ and $K^{\text{vir}}(10) = 1.31$.

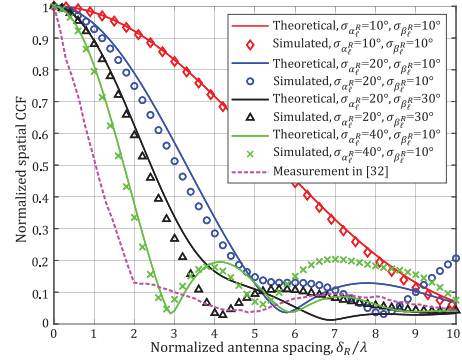
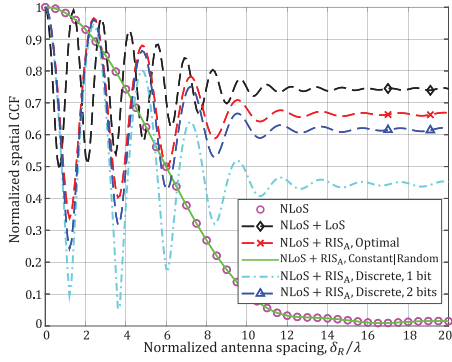


Fig. 7. Normalized spatial CCFs of different components Fig. 8. Normalized spatial CCFs of the proposed model with different RIS reflection phase configurations at $t = 2$ s with different cluster angle spread at $t = 2$ s ($v_T = 5$ m/s, $(v_T = 5$ m/s, $\gamma_T = -\frac{\pi}{6}$, $\eta_T = \frac{\pi}{24}$, $v_R = 2$ m/s, $\gamma_R = \frac{\pi}{6}$). $\gamma_T = -\frac{\pi}{6}$, $\eta_T = \frac{\pi}{24}$, $v_R = 2$ m/s, $\gamma_R = \frac{\pi}{6}$).

Rician fading under discrete and constant reflection phase configurations but with different fading parameters as compared with optimal reflection phase configuration. Moreover, Fig. 6 reveals that the proposed channel model show different fading parameters at different instants, which verifies the non-stationarity of the channel model.

3) *Time-varying Spatial CCF*: In Fig. 7, we compare the spatial CCFs of different components under different RIS reflection phase configurations when the mobile terminals adopts a general mobility model. It can be seen that the channel with optimal and discrete RIS reflection phase configurations shows similar decreasing trend of the spatial CCFs as compared to that of the channel with LoS component, which means that the RIS component behaves similarly to the

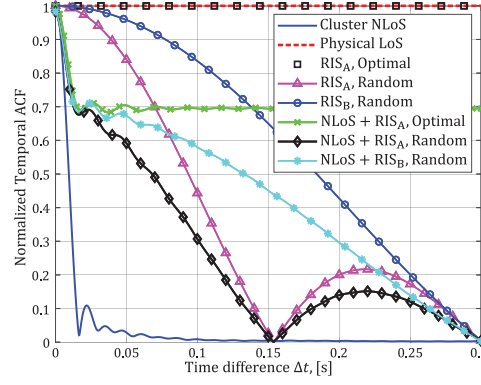


Fig. 9. Normalized temporal ACFs of different components at $t = 2$ s ($v_T = 5$ m/s, $\gamma_T = 0$, $\eta_T = \pi/2$, $v_R = 5$ m/s, $\gamma_R = \pi$).

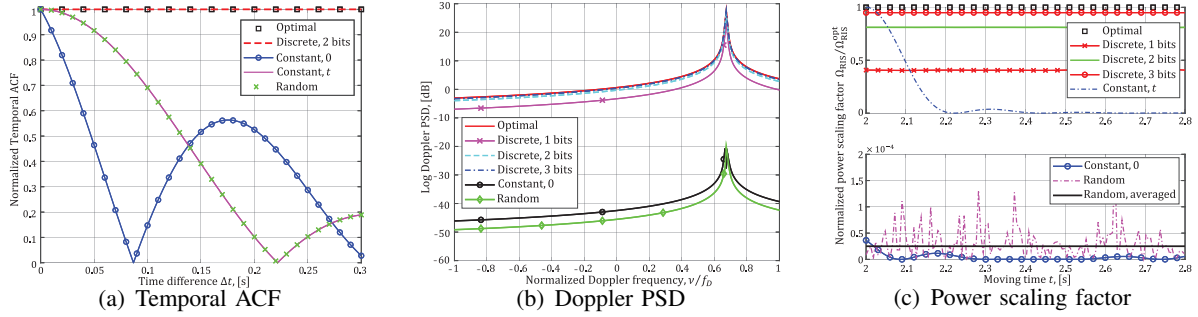


Fig. 10. Channel characteristics of the RIS component in different RIS reflection phase configurations, $t = 2$ s.

physical LoS path. It should be noted that the spatial CCFs of the channel with constant and random reflection phase configuration coincide with the results of the NLoS component owing to the very small power gains. Therefore, although constant and random reflection phase configurations are more benefit for spatial diversity, they have relatively small power gains, thus less helpful. Then, in Fig. 8 we investigate the impact of cluster angle spread on channel spatial CCFs by setting the RIS component as zero [22], where the results show that larger angle spread results in lower spatial correlation of the channel, which meets with the results in [22]. Moreover, the theoretical results in Fig. 8 are in agreement with the simulated results and measurements in [32], thus further validates the effectiveness of the proposed model.

4) *Time-varying Temporal ACF and Doppler PSD:* In Fig. 9, we take a comparison of the channel temporal correlations of different components of the proposed channel model, where the results show RIS_A provides faster decline on temporal ACF than the RIS_B due to larger spatial spread. It can be seen that the RIS component provides the same temporal ACF as the

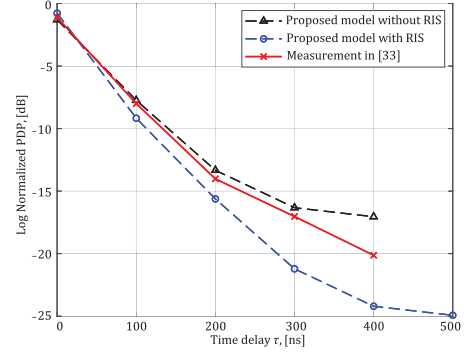
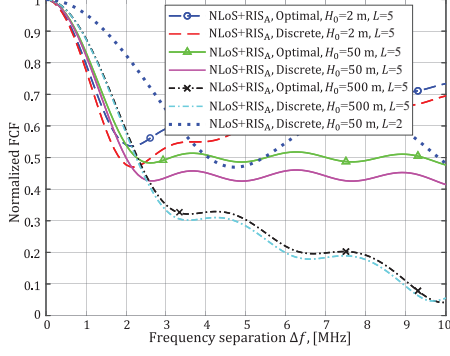


Fig. 11. Normalized FCFs of the proposed channel model with different UAV height and cluster number. Fig. 12. Normalized PDPs of the proposed channel model.

physical LoS path under optimal reflection phase configuration. When the RIS applies random reflection phase configuration, on the contrary, the RIS component provides a cluster NLoS-shaped decline on temporal ACF but with a much slower decreasing trend. Moreover, the results reveal that the existence of RIS will slow down the decline of the temporal correlation of the LoS-obstructed UAV mmWave channel, thus results in longer channel coherence time and less frequently channel estimation. Then, in Fig. 10 we study the impacts of RIS reflection phase configurations on channel temporal ACFs, Doppler PSDs, and RIS power delivering capabilities, where *Constant, t* means $\varphi_{mn}^{\text{const}} = \varphi_{mn}^{\text{opt}}(t)$ with $t = 2$ s in Fig. 10. The results in Figs. 10(a) and (b) show that the constant and random reflection phase configurations behave similarly in both temporal ACFs and Doppler PSDs, whereas the discrete and optimal reflection phase configurations behave similarly in both temporal ACFs and Doppler PSDs, which highlight the advantage of discrete phase configuration. The results in Fig. 10(c) also indicates the discrete reflection phase configuration has the ability to provide a near-optimal performance with several controlling bits and significant reduction in the implementation complexity, which motivates the usage of *discrete* RIS reflection phase configuration.

5) *Time-varying FCF and PDP*: In Fig. 11 we investigate the impact of UAV's height on channel frequency propagation characteristics, where the results indicate that the channel FCF decreases slower when increasing the UAV's height, thus results in larger coherence bandwidth and higher throughput. Also, the results imply that a 2-bit discrete reflection phase configuration can approach the optimal reflection phase configuration well, which is consistent with the results

in Fig. 10. Moreover, we find that the channel with less cluster show higher frequency correlation, and hence larger coherence bandwidth, which is in agreement with the results in [22]. By using (38), we simulate the PDP of the proposed channel model under optimal reflection phase configuration in Fig. 12. The results show that the power is more centered in the first path when the RIS exists, which is similar to the results in [23] with LoS path exists. By setting the RIS component as zero, the proposed channel model reduces to conventional channel model with LoS path obstructed. The well agreement of the PDPs between the proposed model without RIS and measurements in [33] further validates the effectiveness of the proposed channel model.

V. CONCLUSIONS

In this paper, we have developed a 3D non-stationary wideband end-to-end channel model for RIS auxiliary UAV-to-ground mmWave MIMO communications, which has the ability to capture the non-stationarity of UAV channels and the sparsity of mmWave channels. The proposed modeling solution can efficiently describe the physical properties of RIS auxiliary communication channels by modeling the RIS as a virtual cluster and by developing end-to-end CIRs to characterize the physical properties of the underlying propagation channels. The impact of different RIS reflection phase controlling mechanisms on channel statistical properties has been investigated, where the results show that the RIS component behaves like physical LoS path under optimal and discrete reflection phase configurations and a 2-bit discrete reflection phase configuration can approach the performance of optimal reflection phase configuration but with significant reduction in realization complexity. Moreover, the results demonstrate that generally a smaller incident angle and a closer location of RIS to the transceivers can result in higher received power; meanwhile, the fading of the RIS auxiliary channel is generally characterized by Rician fading, whereas by Rayleigh fading when the RIS employs random uniform reflection phase configuration and contains a large number of units. Finally, the agreement between the theoretical and simulated as well as measurement results validates the effectiveness of the proposed channel model, which can inform the design of RIS-assisted communication systems and help researchers for algorithm validations and system performance analyses via simulations.

As a future work, it is important to study the propagation characteristics of RIS auxiliary short-range near-field communications. Moreover, new characteristics in multiple RISs cooperative communications should also be investigated.

APPENDIX A

We define P_t as the transmitting power and G_t as the beamforming gain of the UAV antenna array. Then, the received power of the (m, n) -th RIS unit can be calculated by

$$P_{mn}^{\text{in}}(t) = \frac{P_t G_t}{4\pi \xi_{mn}^T{}^2(t)} \times d_M d_N \cos \beta_{\text{in}}(t), \quad (39)$$

where $\xi_{mn}^T(t) = \xi_{\text{RIS}}^T(t) - k_m d_M \sin \beta_{\text{in}}(t) \cos \alpha_{\text{in}}(t) - k_n d_N \sin \beta_{\text{in}}(t) \cos \alpha_{\text{in}}(t)$ denotes the distance from the center of UAV antenna array to the (m, n) -th RIS unit. Then, the reflected power by the (m, n) -th RIS unit can be expressed as [34]

$$P_{mn}^{\text{out}}(t) = \frac{P_t G_t}{4\pi \xi_{mn}^T{}^2(t)} d_M d_N \cos \beta_{\text{in}}(t) |\chi_{mn}(t) e^{j\varphi_{mn}(t)}|^2. \quad (40)$$

Let G_r be the combining gain of the MR antenna array, thus the effective aperture of the receiving antenna can be expressed as $S_{r,ap} = G_r \lambda^2 / 4\pi$. Then, the received power of the MR from the (m, n) -th RIS unit can be calculated by

$$P_{mn}^r(t) = \frac{P_{mn}^{\text{out}}(t)}{4\pi \xi_{mn}^R{}^2(t)} S_{r,ap}, \quad (41)$$

where $\xi_{mn}^R(t) = \xi_{\text{RIS}}^R(t) - k_m d_M \sin \beta_o(t) \cos \alpha_o(t) - k_n d_N \sin \beta_o(t) \cos \alpha_o(t)$ denotes the distance from the center of MR antenna array to the (m, n) -th RIS unit. By substituting (40) into (41), we can obtain

$$P_{mn}^r(t) = \frac{P_t G_t G_r \lambda^2 d_M d_N \cos \beta_{\text{in}}(t)}{(4\pi)^3 \xi_{mn}^T{}^2(t) \xi_{mn}^R{}^2(t)} |\chi_{mn}(t) e^{j\varphi_{mn}(t)}|^2. \quad (42)$$

As indicated in [35], the received power $P_{mn}^r(t)$ can also be expressed as

$$P_{mn}^r(t) = \frac{|E_{mn}^r(t)|^2}{2\eta} S_{r,ap}, \quad (43)$$

where η is the intrinsic impedance ($\simeq 120\pi$ ohms for free-space), and $E_{mn}^r(t)$ is the received radiation electric field. By combining (42) and (43), $E_{mn}^r(t)$ can be solved as

$$E_{mn}^r(t) = \sqrt{\frac{2\eta P_t G_t G_r \lambda^2 d_M d_N \cos \beta_{\text{in}}(t)}{(4\pi)^3 S_{r,ap}}} \times \frac{\chi_{mn}(t) e^{j\varphi_{mn}(t)}}{\xi_{mn}^T(t) \xi_{mn}^R(t)} \times e^{-j\frac{2\pi}{\lambda}(\xi_{mn}^T(t) + \xi_{mn}^R(t))} \\ \times e^{j\frac{2\pi}{\lambda}v_T t \left(\cos(\alpha_{\text{RIS}}^T(t) - \gamma_T) \cos \beta_{\text{RIS}}^T(t) \cos \eta_T + \sin \beta_{\text{RIS}}^T(t) \sin \eta_T \right)} e^{j\frac{2\pi}{\lambda}v_R t \cos(\alpha_{\text{RIS}}^R(t) - \gamma_R) \cos \beta_{\text{RIS}}^R(t)}. \quad (44)$$

The superimposed received electric field can be calculated by $E_r(t) = \sum_{m=1}^M \sum_{n=1}^N E_{mn}^r(t)$. Similar to (43), the MR received reflection power from RIS can be expressed as

$$P_r(t) = \frac{|E_r(t)|^2}{2\eta} S_{r,ap}$$

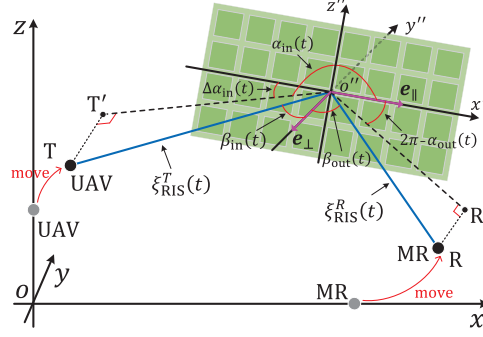


Fig. B-1. Illustration of the incident and reflected angles on RIS. T and R denote the positions of UAV and MR, respectively, whereas T' and R' are their projections on the $x''-y''-z''$ plane, respectively. The $x''-y''-z''$ is established over the RIS and can be derived by rotating $x'-y'-z'$ in Fig. 2(b) by a horizontal rotation angle of θ_I and a vertical rotation angle of ϵ_I , respectively.

$$= P_r^{free}(t) \times \frac{d_M d_N \cos \beta_{in}(t) (\xi_{RIS}^T(t) + \xi_{RIS}^R(t))^2}{4\pi} \left| \sum_{m=1}^M \sum_{n=1}^N \frac{\chi_{mn}(t) e^{j(\varphi_{mn}(t) - \varphi_{mn}^{dis}(t))}}{\xi_{mn}^T(t) \xi_{mn}^R(t)} \right|^2, \quad (45)$$

where $P_r^{free}(t) = \frac{P_t G_t G_r \lambda^2}{(4\pi)^2 (\xi_{RIS}^T(t) + \xi_{RIS}^R(t))^2}$ is the received power of the same-distance free path and $\varphi_{mn}^{dis}(t)$ is the distance-related phase term which is related with index m and n , that is,

$$\begin{aligned} \varphi_{mn}^{dis}(t) = & -\frac{2\pi}{\lambda} k_m d_M (\sin \beta_{in}(t) \cos \alpha_{in}(t) + \sin \beta_{out}(t) \cos \alpha_{out}(t)) \\ & - \frac{2\pi}{\lambda} k_n d_N (\sin \beta_{in}(t) \sin \alpha_{in}(t) + \sin \beta_{out}(t) \sin \alpha_{out}(t)), \end{aligned} \quad (46)$$

where $k_m = \frac{2m-M-1}{2}$ and $k_n = \frac{2n-N-1}{2}$. Therefore, Theorem 1 holds.

APPENDIX B

In Fig. B-1, we illustrate the time-varying incident and reflected angles on RIS, which are defined based on the local coordinate system $x''-y''-z''$. Then, the unit vector along the positive direction of x'' -axis and that along the negative direction of y'' -axis can be expressed as $\mathbf{e}_{\parallel} = [\cos \theta_I, \sin \theta_I, 0]^T$ and $\mathbf{e}_{\perp} = [\sin \theta_I \cos \epsilon_I, -\cos \theta_I \cos \epsilon_I, -\sin \epsilon_I]^T$, respectively. At time t , the positions of UAV and MR are at points $\mathbf{T} = (v_T t \cos \eta_T \cos \gamma_T, v_T t \cos \eta_T \sin \gamma_T, H_0 + v_T t \sin \eta_T)$ and $\mathbf{R} = (\xi_R + v_R t \cos \gamma_R, v_R t \sin \gamma_R, 0)$, respectively. Therefore, the distance vectors from the center of RIS to UAV and to MR, denoted by $\mathbf{d}_{o''}^T(t)$ and $\mathbf{d}_{o''}^R(t)$, respectively, can be expressed as

$$\mathbf{d}_{o''}^T(t) = \mathbf{T} - \mathbf{o}'' = \begin{bmatrix} v_T t \cos \eta_T \cos \gamma_T - x_I \\ v_T t \cos \eta_T \sin \gamma_T - y_I \\ H_0 + v_T t \sin \eta_T - z_I \end{bmatrix}, \quad (47)$$

$$\mathbf{d}_{o''}^R(t) = \mathbf{R} - o'' = \begin{bmatrix} \xi_R + v_R t \cos \gamma_R - x_I \\ v_R t \sin \gamma_R - y_I \\ -z_I \end{bmatrix}, \quad (48)$$

where $\|\mathbf{d}_{o''}^T(t)\| = \xi_{\text{RIS}}^T(t)$ and $\|\mathbf{d}_{o''}^R(t)\| = \xi_{\text{RIS}}^R(t)$. Next, we can derive the normal incident angle from UAV to RIS and normal reflected angle from RIS to MR as

$$\begin{aligned} \beta_{\text{in}}(t) &= \arccos \frac{\mathbf{e}_{\perp}^T \cdot \mathbf{d}_{o''}^T(t)}{\|\mathbf{e}_{\perp}\| \cdot \|\mathbf{d}_{o''}^T(t)\|} \\ &= \arccos \frac{(r_T^x(t) - x_I) \sin \theta_I \cos \epsilon_I - (r_T^y(t) - y_I) \cos \theta_I \cos \epsilon_I - (H_0 + r_T^z(t) - z_I) \sin \epsilon_I}{\xi_{\text{RIS}}^T(t)}, \end{aligned} \quad (49)$$

$$\begin{aligned} \beta_{\text{out}}(t) &= \arccos \frac{\mathbf{e}_{\perp}^T \cdot \mathbf{d}_{o''}^R(t)}{\|\mathbf{e}_{\perp}\| \cdot \|\mathbf{d}_{o''}^R(t)\|} \\ &= \arccos \frac{(\xi_R + r_R^x(t) - x_I) \sin \theta_I \cos \epsilon_I - (r_R^y(t) - y_I) \cos \theta_I \cos \epsilon_I + z_I \sin \epsilon_I}{\xi_{\text{RIS}}^R(t)}. \end{aligned} \quad (50)$$

Once the normal incident $\beta_{\text{in}}(t)$ and reflected $\beta_{\text{out}}(t)$ angles are obtained, the distance vectors from o'' to projection points T' and R' , denoted by $\mathbf{d}_{o''}^{T'}(t)$ and $\mathbf{d}_{o''}^{R'}(t)$, respectively, can be derived by

$$\begin{aligned} \mathbf{d}_{o''}^{T'}(t) &= \mathbf{d}_{o''}^T(t) - \xi_{\text{RIS}}^T(t) \cos \beta_{\text{in}}(t) \cdot \mathbf{e}_{\perp} \\ &= \begin{bmatrix} v_T t \cos \eta_T \cos \gamma_T - x_I - \xi_{\text{RIS}}^T(t) \cos \beta_{\text{in}}(t) \sin \theta_I \cos \epsilon_I \\ v_T t \cos \eta_T \sin \gamma_T - y_I + \xi_{\text{RIS}}^T(t) \cos \beta_{\text{in}}(t) \cos \theta_I \cos \epsilon_I \\ H_0 + v_T t \sin \eta_T - z_I + \xi_{\text{RIS}}^T(t) \cos \beta_{\text{in}}(t) \sin \epsilon_I \end{bmatrix}, \end{aligned} \quad (51)$$

$$\begin{aligned} \mathbf{d}_{o''}^{R'}(t) &= \mathbf{d}_{o''}^R(t) - \xi_{\text{RIS}}^R(t) \cos \beta_{\text{out}}(t) \cdot \mathbf{e}_{\perp} \\ &= \begin{bmatrix} \xi_R + v_R t \cos \gamma_R - x_I - \xi_{\text{RIS}}^R(t) \cos \beta_{\text{out}}(t) \sin \theta_I \cos \epsilon_I \\ v_R t \sin \gamma_R - y_I + \xi_{\text{RIS}}^R(t) \cos \beta_{\text{out}}(t) \cos \theta_I \cos \epsilon_I \\ -z_I + \xi_{\text{RIS}}^R(t) \cos \beta_{\text{out}}(t) \sin \epsilon_I \end{bmatrix}. \end{aligned} \quad (52)$$

Therefore, the azimuth incident angle from UAV to RIS, that is, $\alpha_{\text{in}}(t)$, and the azimuth reflected angle from RIS to MR, that is, $\alpha_{\text{out}}(t)$, can be respectively expressed as

$$\alpha_{\text{in}}(t) = \begin{cases} \pi - \Delta\alpha_{\text{in}}(t), & \text{if } H_0 + v_T t \sin \eta_T - z_I + \xi_{\text{RIS}}^T(t) \cos \beta_{\text{in}}(t) \sin \epsilon_I > 0 \\ \pi + \Delta\alpha_{\text{in}}(t), & \text{if } H_0 + v_T t \sin \eta_T - z_I + \xi_{\text{RIS}}^T(t) \cos \beta_{\text{in}}(t) \sin \epsilon_I \leq 0 \end{cases}, \quad (53)$$

$$\begin{aligned}
\alpha_{\text{out}}(t) &= 2\pi - \arccos \frac{\mathbf{e}_{\parallel}^T \cdot \mathbf{d}_{o''}^{\text{R}'}(t)}{\|\mathbf{e}_{\parallel}\| \cdot \|\mathbf{d}_{o''}^{\text{R}'}(t)\|} \\
&= 2\pi - \arccos \frac{(\xi_R + v_R t \cos \gamma_R - x_I) \cos \theta_I + (v_R t \sin \gamma_R - y_I) \sin \theta_I}{\|\mathbf{d}_{o''}^{\text{R}'}(t)\|}, \tag{54}
\end{aligned}$$

where $\Delta\alpha_{\text{in}}(t)$ is expressed as

$$\begin{aligned}
\Delta\alpha_{\text{in}}(t) &= \arccos \frac{(-\mathbf{e}_{\parallel})^T \cdot \mathbf{d}_{o''}^{\text{T}'}(t)}{\|(-\mathbf{e}_{\parallel})\| \cdot \|\mathbf{d}_{o''}^{\text{T}'}(t)\|} \\
&= \arccos \frac{(x_I - v_T t \cos \eta_T \cos \gamma_T) \cos \theta_I + (y_I - v_T t \cos \eta_T \sin \gamma_T) \sin \theta_I}{\|\mathbf{d}_{o''}^{\text{T}'}(t)\|}. \tag{55}
\end{aligned}$$

APPENDIX C

Let us take the propagation between the $(p \rightarrow q)$ -th transmit-receive antenna pair as an example. We assume that an unmodulated carrier is transmitted, i.e., $s(t) = 1$, then the received complex envelope without noise can be obtained by convolving the transmitted signal $s(t)$ with the channel response $h_{pq}(t, \tau, \Theta_T, \Theta_R)$ as [30]

$$r(t) = \int_{-\infty}^{\infty} h_{pq}(t, \tau, \Theta_T, \Theta_R) s(t - \tau) d\tau = h_{pq}^{\text{RIS}}(t) + \sum_{\ell=1}^L h_{\ell,pq}(t). \tag{56}$$

With the phases $\varphi_{\ell,i}$ in (6) being independent and identically distributed random variables as well as the Central Limit Theorem, $h_{\ell,pq}(t)$ approaches a Rayleigh process with zero mean and variance of $P_{\ell}(t)$ when I is large enough [23]. Moreover, with the uncorrelated scattering assumption [30], $g(t) = \sum_{\ell=1}^L h_{\ell,pq}(t)$ is the summation of L independent Rayleigh processes with zero mean and variance of $\sum_{\ell=1}^L P_{\ell}(t)$, that is, $\mathbb{E}\{g(t)\} = 0$ and $\text{Var}\{g(t)\} = \sum_{\ell=1}^L P_{\ell}(t)$.

The RIS component $h_{pq}^{\text{RIS}}(t) = \text{Re}\{h_{pq}^{\text{RIS}}(t)\} + j \cdot \text{Im}\{h_{pq}^{\text{RIS}}(t)\}$ is a deterministic process, then we can rewrite (56) as

$$\text{Re}\{r(t)\} + j \cdot \text{Im}\{r(t)\} = \text{Re}\{h_{pq}^{\text{RIS}}(t)\} + \text{Re}\{g(t)\} + j \cdot (\text{Im}\{h_{pq}^{\text{RIS}}(t)\} + \text{Im}\{g(t)\}). \tag{57}$$

Accordingly, we can observe that the real part $\text{Re}\{r(t)\}$ and imaginary part $\text{Im}\{r(t)\}$ are Gaussian random processes with different mean values $\text{Re}\{h_{pq}^{\text{RIS}}(t)\}$ and $\text{Im}\{h_{pq}^{\text{RIS}}(t)\}$, respectively, but the same variance $\frac{1}{2} \sum_{\ell=1}^L P_{\ell}(t)$. Moreover, the correlation function between $\text{Re}\{r(t)\}$ and $\text{Im}\{r(t)\}$ can be expressed as

$$\begin{aligned}
\text{Cov}(\text{Re}\{r(t)\}, \text{Im}\{r(t)\}) &= \mathbb{E}\left\{(\text{Re}\{r(t)\} - \text{Re}\{h_{pq}^{\text{RIS}}(t)\})^* \cdot (\text{Im}\{r(t)\} - \text{Im}\{h_{pq}^{\text{RIS}}(t)\})\right\} \\
&= 0. \tag{58}
\end{aligned}$$

Therefore, $\text{Re}\{r(t)\}$ and $\text{Im}\{r(t)\}$ are two independent Gaussian random processes with non-zero means and same variance. Thus, $r(t)$ is a Rice process and the fading of the proposed channel model is characterized by Rician fading with the non-centrality parameter $[\text{Re}\{h_{pq}^{\text{RIS}}(t)\}]^2 + [\text{Im}\{h_{pq}^{\text{RIS}}(t)\}]^2 = |h_{pq}^{\text{RIS}}(t)|^2 = \Omega_{\text{RIS}}(t)$. Thus, Corollary 2 holds.

REFERENCES

- [1] W. Saad, M. Bennis, and M. Z. Chen, "A vision of 6G wireless systems: applications, trends, technologies, and open research problems," *IEEE Netw.*, vol. 34, no. 3, pp. 134-142, Jun. 2020.
- [2] J. Liu *et al.*, "Space-air-ground integrated network: a survey," *IEEE Commun. Surveys Tuts.*, vol. 20, no. 4, pp. 2714-2741, 4th Quart., 2018.
- [3] M. Mozaffari *et al.*, "A tutorial on UAVs for wireless networks: applications, challenges, and open problems," *IEEE Commun. Surveys Tuts.*, vol. 21, no. 3, pp. 2334-2360, 3th Quart., 2019.
- [4] Z. Y. Xiao, P. F. Xia, and X.-G. Xia, "Enabling UAV cellular with millimeter-wave communication: potentials and approaches," *IEEE Commun. Mag.*, vol. 54, no. 5, pp. 66-73, May 2016.
- [5] E. Basar *et al.*, "Wireless communications through reconfigurable intelligent surfaces," *IEEE Access*, vol. 7, pp. 116753-116773, Aug. 2019.
- [6] S. X. Li *et al.*, "Reconfigurable intelligent surface assisted UAV communication: joint trajectory design and passive beamforming," *IEEE Wireless Commun. Lett.*, vol. 9, no. 5, pp. 716-720, May 2020.
- [7] H. Q. Lu *et al.*, "Enabling panoramic full-angle reflection via aerial intelligent reflecting surface," in *Proc. IEEE ICC*, Dublin, Ireland, Jun. 2020.
- [8] C. D. Pradhan *et al.*, "Hybrid precoding design for reconfigurable intelligent surface aided mmWave communication systems," *IEEE Wireless Commun. Lett.*, vol. 9, no. 7, pp. 1041-1045, Jul. 2020.
- [9] N. S. Perovic, M. Di Renzo, and M. F. Flanagan, "Channel capacity optimization using reconfigurable intelligent surfaces in indoor mmWave environments," in *Proc. IEEE ICC*, Dublin, Ireland, Jun. 2020.
- [10] W. K. Tang *et al.*, "Wireless communications with programmable metasurface: new paradigms, opportunities, and challenges on transceiver design," *IEEE Wireless Commun.*, vol. 27, no. 2, pp. 180-187, Apr. 2020.
- [11] T. W. Hou *et al.*, "Reconfigurable intelligent surface aided NOMA networks," *IEEE J. Sel. Areas Commun.*, vol. 38, no. 11, pp. 2575-2588, Nov. 2020.
- [12] E. Basar, "Reconfigurable intelligent surface-based index modulation: a new beyond MIMO paradigm for 6G," *IEEE Trans. Commun.*, vol. 68, no. 5, pp. 3187-3196, May 2020.
- [13] S. Hu, F. Rusek, and O. Edfors, "Beyond massive MIMO: the potential of positioning with large intelligent surfaces," *IEEE Trans. Signal Process.*, vol. 66, no. 7, pp. 1761-1774, Apr. 2018.
- [14] J. G. He *et al.*, "Adaptive beamforming design for mmWave RIS-aided joint localization and communication," in *Proc. IEEE WCNC Workshops*, Seoul, Korea (South), Apr. 2020, pp. 1-6.
- [15] O. Ozdogan, E. Bjornson, and E. G. Larsson, "Intelligent reflecting surfaces: physics, propagation, and pathloss modeling," *IEEE Wireless Commun. Lett.*, vol. 9, no. 5, pp. 581-585, May 2020.
- [16] F. H. Danufane *et al.*, "On the path-loss of reconfigurable intelligent surfaces: an approach based on Green's theorem applied to vector fields," *IEEE Trans. Commun.*, DOI: 10.1109/TCOMM.2021.3081452.

- [17] J. C. B. Garcia, A. Sibille, and M. Kamoun, "Reconfigurable intelligent surfaces: bridging the gap between scattering and reflection," *IEEE J. Sel. Areas Commun.*, vol. 38, no. 11, pp. 2538-2547, Nov. 2020.
- [18] W. K. Tang *et al.*, "Wireless communications with reconfigurable intelligent surface: path loss modeling and experimental measurement," *IEEE Trans. Wireless Commun.*, vol. 20, no. 1, pp. 421-439, Jan. 2021.
- [19] M. Najafi *et al.*, "Physics-based modeling and scalable optimization of large intelligent reflecting surfaces," *IEEE Trans. Commun.*, vol. 69, no. 4, pp. 2673-2691, Apr. 2021.
- [20] H. Jiang *et al.*, "A general wideband non-stationary stochastic channel model for intelligent reflecting surface-assisted MIMO communications," *IEEE Trans. Wireless Commun.*, DOI: 10.1109/TWC.2021.3066806.
- [21] E. Basar and I. Yildirim "Reconfigurable intelligent surfaces for future wireless networks: a channel modeling perspective," *IEEE Wireless Commun.*, DOI: 10.1109/MWC.001.2000338.
- [22] R. He *et al.*, "Geometrical-based modeling for millimeter-wave MIMO mobile-to-mobile channels," *IEEE Trans. Veh. Technol.*, vol. 67, no. 4, pp. 2848-2863, Apr. 2018.
- [23] B. Xiong *et al.*, "Novel multi-mobility V2X channel model in the presence of randomly moving clusters," *IEEE Trans. Wireless Commun.*, vol. 20, no. 5, pp. 3180-3195, May 2021.
- [24] *Study on Channel Model for Frequencies from 0.5 to 100 GHz*, 3GPP TR 38.901, ver. 16.1.0, Release 16, Dec. 2019.
- [25] H. Jiang *et al.*, "A 3-D non-stationary wideband geometry-based channel model for MIMO vehicle-to-vehicle communications in tunnel environments," *IEEE Trans. Veh. Technol.*, vol. 68, no. 7, pp. 6257-6271, Jul. 2019.
- [26] M. K. Samimi and T. S. Rappaport, "3D millimeter-wave statistical channel model for 5G wireless system design," *IEEE Trans. Microwave Theory and Techniques*, vol. 64, no. 7, pp. 2207-2225, Jul. 2016.
- [27] N. F. Yu *et al.*, "Light propagation with phase discontinuities: generalized laws of reflection and refraction," *Science*, vol. 334, no. 6054, pp. 333-337, Oct. 2011.
- [28] Q. Wu and R. Zhang, "Intelligent reflecting surface enhanced wireless network: joint active and passive beamforming design," in *Proc. IEEE GLOBECOM*, Abu Dhabi, United Arab Emirates, Dec. 2018, pp. 1-6.
- [29] H. T. Chang *et al.*, "A novel non-stationary 6G UAV-to-Ground wireless channel model with 3D arbitrary trajectory changes," *IEEE Int. Things J.*, vol. 8, no. 12, pp. 9865-9877, Jun. 2021.
- [30] Andrea Goldsmith, *Wireless Communications*, Cambridge University Press, 2005.
- [31] S. Wu *et al.*, "A general 3-D non-stationary 5G wireless channel model," *IEEE Trans. Commun.*, vol. 66, no. 7, pp. 3065-3078, Jul. 2018.
- [32] S. Payami and F. Tufvesson, "Channel measurements and analysis for very large array systems at 2.6 GHz," in *Proc. EUCAP*, Prague, Czech Republic, Mar. 2012, pp. 433-437.
- [33] M. K. Samimi and T. S. Rappaport, "3-D statistical channel model for millimeter-wave outdoor mobile broadband communications," in *Proc. IEEE ICC*, London, UK, Jun. 2015, pp. 2430-2436.
- [34] C. A. Balanis, *Antenna Theory: Analysis and Design*, John Wiley & Sons, Inc., Hoboken, New Jersey, 2016.
- [35] W. L. Stutzman and G. A. Thiele, *Antenna Theory and Design*, John Wiley & Sons, Inc., 2013.